

MODELING PROPAGATION LOSS IN SHALLOW WATER USING A  
FINITE DIFFERENCE PARABOLIC EQUATION

A THESIS SUBMITTED TO THE GRADUATE DIVISION OF THE  
UNIVERSITY OF HAWAII IN PARTIAL FULFILLMENT  
OF THE REQUIREMENTS FOR THE DEGREE OF

MASTER OF SCIENCE

IN GEOLOGY AND GEOPHYSICS

DECEMBER 1982

BY

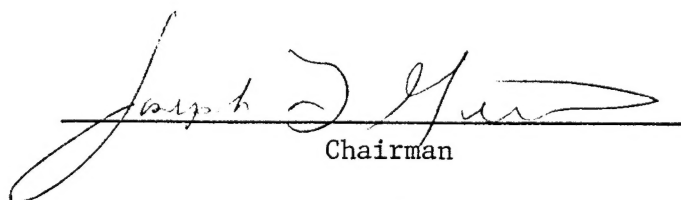
Brian Takashi Iwatake

Thesis Committee:

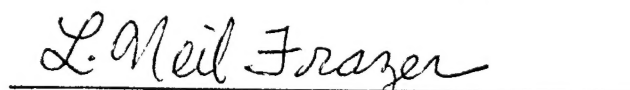
Joseph F. Gettrust, Chairman  
Thomas M. Brocher  
L. Neil Frazer  
Gerard J. Fryer

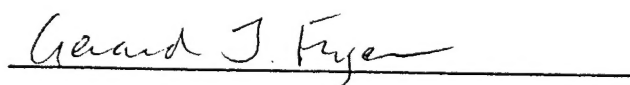
We certify that we have read this thesis and that in our opinion it is satisfactory in scope and quality as a thesis for the degree of Master of Science in Geology and Geophysics.

## THESIS COMMITTEE

  
Chairman







## ACKNOWLEDGEMENTS

This thesis was funded by the Earth and Environmental Physics Program, Office of Naval Research. Mark Odegard, Dave Byrne, Grant Blackinton, Bill Ichinose, Pat Cooper, and George Sutton collected the data for the Hawaii Institute of Geophysics, in cooperation with Western Electric Company and the U.S. Navy. Grant Blackinton and Ken Hiraki resurrected electronic equipment necessary to play back the data. Mobil Oil Company, Ltd. of Canada provided airgun shot times and location information. Mike Ryan stimulated my interest in the use of finite differences for solving physical problems. Ed Berg reviewed my thesis on very short notice. Tom Brocher was a source of encouragement in my work, and I hope that his efforts to make this thesis readable were not in vain. To the present and former inhabitants and frequenters of the third floor - thanks for making life a little more bearable. Lastly, I wish to thank my parents for their support over the years.

## ABSTRACT

An implicit finite difference version of the 15<sup>0</sup> parabolic equation first developed by Claerbout was used to model acoustic wave propagation in shallow water. The algorithm uses a variable grid spacing in the depth as well as range direction, resulting in rapid execution. The water-sediment interface was simulated by an Epstein layer. An attempt to model propagation loss data on the continental slope and shelf near Nova Scotia was unsuccessful because of a lack of adequate environmental data, as well as deficiencies in the modeling method. However, from modeling it was found that the sediment properties controlled propagation loss near the cutoff frequency.

## TABLE OF CONTENTS

ACKNOWLEDGEMENTS . . . . .	iii
ABSTRACT . . . . .	iv
LIST OF TABLES . . . . .	vi
LIST OF ILLUSTRATIONS. . . . .	vii
I. INTRODUCTION. . . . .	1
II. DEVELOPMENT OF NUMERICAL MODELING TECHNIQUES. . . . .	4
Derivation of the parabolic approximation to to the wave equation. . . . .	4
An implicit finite difference formulation of the parabolic equation. . . . .	8
Source modeling . . . . .	16
Including attenuation in the parabolic equation . . . . .	16
Modeling the ocean-sediment interface . . . . .	17
III. MODELING PROPAGATION ON A CONTINENTAL SLOPE . . . . .	23
Field experiment. . . . .	23
Physical properties of the slope. . . . .	26
Constructing a velocity-depth model . . . . .	29
An Epstein layer for the water-sediment interface . . . . .	31
Choosing a computational grid . . . . .	35
The parabolic equation model output . . . . .	40
Comparison of observed and predicted propagation loss . . . . .	45
IV. MODELING DATA FROM A CONTINENTAL SHELF. . . . .	46
Bathymetry . . . . .	46
Constructing a velocity-depth model . . . . .	48
Comparison of data to model at 25 Hz. . . . .	54
Comparison of data to model at 10 Hz. . . . .	58
V. DISCUSSION ON SOURCES OF MODELING ERROR . . . . .	61
VI. SUMMARY . . . . .	64
APPENDIX A. EPSTEIN LAYER REFLECTIVITY FUNCTION . . . . .	66
APPENDIX B. RAYTRACING ON THE CONTINENTAL SLOPE . . . . .	69
APPENDIX C. HEAD WAVE . . . . .	75
APPENDIX D. SEDIMENT VELOCITY FROM APPARENT VELOCITIES. . . . .	82
REFERENCES . . . . .	85

## LIST OF TABLES

Table		Page
1	Finite difference grid spacings for modeling propagation on the continental slope near Nova Scotia. . . . .	36
2	Finite difference grid spacings for modeling propagation on the Scotian shelf . . . . .	55

## LIST OF ILLUSTRATIONS

Figure		Page
1	The index of refraction squared for the symmetrical component of the Epstein layer, The index of refraction squared for the transitional component . . . . .	20
2	Location of TOBS 3 and SUS charge line on the Scotian continental slope . . . . .	25
3	Sound velocity profiles in the water column. . . . .	27
4	SUS charge arrivals on the Scotian continental slope . . .	28
5	Geoacoustic parameters for modeling propagation on the Scotian slope, The equivalent Epstein layer model of the ocean bottom . .	32
6	Rayleigh and Epstein reflection coefficient and phase for the ocean bottom of Figure 5. . . . .	34
7	Constant grid spacing model, Variable grid spacing. . . . .	38
8	Intensity of the 25 Hz parabolic equation wave field . . .	42
9	Observed 25 Hz SUS charge signal level versus range, Computed parabolic equation wavefield at 25 Hz . . . . .	43
10	Comparison of the outputs of the parabolic equation model at 25 Hz for the variable and constant grid spacing .	44
11	Bathymetry beneath airgun shot points. . . . .	47
12	Airgun data from the Scotian shelf . . . . .	49
13	Geoacoustic model for the airgun shot line on the Scotian shelf . . . . .	52
14	Rayleigh and Epstein reflectivities at 25 Hz for the ocean bottom and sub-bottom interfaces, Same for 10 Hz . . . . .	53

## LIST OF ILLUSTRATIONS (Continued)

Figure		Page
15	Observed 25 Hz airgun signal level versus range, 25 Hz parabolic equation output for the Figure 13 model, Parabolic equation output for sediment trough model. . . .	56
16	10 Hz signal levels, Parabolic equation output for the Figure 13 model at 10 Hz, 10 Hz output for above model with sediment trough, 10 Hz sediment trough model with $1 \text{ s}^{-1}$ velocity gradient .	59
17	One bottom bounce ray paths from TOBS 3. . . . .	72
18	Double bottom bounce ray paths from TOBS 3 . . . . .	73
19	Triple bottom bounce ray paths from TOBS 3 . . . . .	74
20	Large SUS charge shots originating upslope from TOBS 3, Shots originating downslope from TOBS 3. . . . .	76
21	Geometry for ray paths occurring at critical incidence . .	77
22	First break amplitudes versus computed bottom incident angle for shots on downslope side of TOBS 3, Difference between the computed horizontal range and the range from shipboard navigation . . . . .	80
23	First break amplitudes versus computed bottom incident angle for shots upslope from the receiver, Difference between computed horizontal range and the range from shipboard navigation . . . . .	81
24	Raypath at critical incidence. . . . .	84



## I. INTRODUCTION

Models for the propagation of underwater sound in shallow water are complicated by the interaction with the ocean bottom. When the propagation is range-dependent, the models become even more complex. One method which has been investigated as a tool for analyzing shallow water problems is the parabolic equation technique [Lee and Gilbert, 1982]. Since the parabolic equation is itself an approximation to the wave equation, however, special techniques must be used to model acoustic interfaces. This thesis is devoted to the development of a parabolic equation method for modeling propagation loss in a range-dependent shallow water environment. The method is tested by attempting to model actual data recorded in two separate shallow water environments.

Explosive signals generated on the continental shelf and slope near Nova Scotia [Brocher et al., 1981] were analyzed to study acoustic propagation in a range-dependent shallow water environment. The data were recorded by ocean bottom sensors at two water depths. The shallow sensor, at a depth of 67 m, was situated in a region of bottom-limited sound propagation. The other sensor was on the continental slope in 1301 m of water. Seismic propagation loss measurements were obtained from the recorded signals [Brocher et al., 1982]. With geoacoustic models of the water column and sediment structure obtained from various

sources, the parabolic equation was used to model the observed propagation loss.

The parabolic equation is a useful means of calculating long range low frequency acoustic propagation when the raypath turning points occur within the water column [Hanna, 1976; Hanna and Rost, 1981]. This type of propagation usually occurs in a deep ocean with a well defined sound channel. In shallower areas, where bottom interacting paths are present, the parabolic equation method has been less successful [Lee and Gilbert, 1982]. As a result, there is a lack of literature describing parabolic equation modeling of actual shallow water propagation loss data. The difficulty stems from the discontinuous change in velocity and density at the bottom of the ocean. Frisk et al. [1981] derived a parabolic equation technique that accurately modeled the water-sediment interface for single bottom bounce paths in the North Atlantic, but this technique is not applicable to multi-bounce paths. This thesis presents a more general method of treating acoustic interfaces for calculations based on the parabolic equation.

Normal mode theory gives an exact solution to the wave equation in all horizontally stratified media. However, modifying the normal mode technique to take into account range-dependent variation in acoustic media has met with limited success [Graves et al., 1975]. In contrast with normal modes, the parabolic equation is derived from the wave equation without recourse to separation of variables. Thus, the parabolic equation technique is not restricted to the range-independent environment. For the same reason, mode coupling, a phenomenon

associated with sloping bottoms and other two dimensional media, is handled by the parabolic equation [Jensen and Kuperman, 1980]. In spite of its difficulty with interfaces, the parabolic equation's capability to solve range-dependent problems and its correct modeling of mode coupling make it a natural candidate for modeling shallow water acoustic propagation.

McDaniel [1975b] and Lee et al. [1981] devised implicit finite difference algorithms to solve the parabolic equation. Another method introduced by Tappert and Hardin combines the use of the Fourier transform with a finite-difference operation [Tappert, 1977]. Of these two techniques, the implicit finite difference method was selected for the modeling reported here because it can be used with a variety of boundary conditions [DiNapoli and Deavenport, 1979]. Another advantage of implicit finite differences is faster execution. McDaniel [1975b] found this method to be significantly faster than that of Tappert and Hardin. Here, we use an implicit finite difference algorithm to model acoustic wave propagation. A variable grid spacing is used that permits propagation loss models to be computed in less time.

## II. DEVELOPMENT OF NUMERICAL MODELING TECHNIQUES

Derivation of the parabolic approximation to the wave equation

The wave equation using the Laplacian operator  $\nabla^2$ , with velocity  $c$ , and the field variable being pressure  $p$  is

$$\nabla^2 p - \frac{1}{c^2} p_{tt} = 0 \quad . \quad [1]$$

Inserting a continuous sinusoidal time dependence and changing to cylindrical coordinates with no azimuthal dependence results in the Helmholtz or reduced wave equation,

$$p_{rr} + \frac{1}{r} p_r + p_{zz} + k^2 p = 0 \quad , \quad [2]$$

where  $k = k(z,r)$ ,  $c = c(z,r)$ ,  $k = \omega/c$ ,  $\omega = 2\pi f$ . The range,  $r$ , is in the principal direction of propagation and  $z$  is depth, positive downward. Since equation [2] is an elliptic partial differential equation with second derivatives in both  $r$  and  $z$ , it is difficult to solve numerically. Some approximations will be made in order to reduce equation [2] to a simpler form. In addition, two changes of variables will serve to decrease the spatial variation of the computed wavefield, resulting in less numerical error.

It is usual to normalize for cylindrical spreading by introducing

$$p = r^{-1/2} v , \quad [3]$$

which gives

$$v_{rr} + v_{zz} + \left( k^2 - \frac{1}{4r^2} \right) v = 0 . \quad [4]$$

Next, a far-field approximation can be made by neglecting the term  $-1/(4r^2)$  since  $v/r^2$  will be much smaller than  $k^2 v$  for ranges on the order of a few wavelengths or greater. Using a "square-root operator" and binomial expansion [Claerbout, 1970b] or splitting matrix [McDaniel, 1975b], equation [4] may be reduced to

$$v_r = i \left( k + \frac{1}{2k} \frac{\partial^2}{\partial z^2} \right) v . \quad [5]$$

The solution to this parabolic equation represents an outward traveling wave field. The loss of the wavefield second derivative with respect to  $r$  forces a restriction on field gradients that can be treated using this approximation. The equation of the inward traveling wave field has been decoupled from equation [5]. In the splitting matrix technique, a matrix equation arises with terms that cause coupling between the outward and inward traveling waves [Corones, 1975]. These terms are then explicitly deleted to give equation [5]. Physically, coupling manifests itself as back-reflection.

A constant "average" wavenumber  $k_0 = \omega/c_0$  is chosen and the following change of variable is used

$$v = u \exp[ik_0 r] \quad . \quad [6]$$

The new field variable  $u$  changes slowly with range. This result allows larger step sizes in the numerical implementation of the parabolic equation. The effect of the substitution is like moving the coordinate system at the constant velocity  $c_0 = \omega/k_0$  [Volk, 1975]. In practice,  $k_0$  is selected so that  $c_0$  is near the average velocity of the acoustic medium. Inserting equation [6] into equation [5] gives the final parabolic equation,

$$u_r = (i(k - k_0) + \frac{i}{2k} \frac{\partial^2}{\partial z^2})u \quad , \quad [7]$$

which is the basis for the computer model presented in this thesis.

The following comments pertain to both equation [7] and the similar Tappert and Hardin [Tappert, 1977] equation. The parabolic equation [7] gives an accurate solution for the propagation of a single normal mode with wavenumber  $k_0$  if the waveguide does not induce coupling into other modes [Fitzgerald, 1975]. For modes of propagation with values of wavenumber  $k$  departing from  $k_0$  (or phase velocity  $c$  differing from  $c_0$ ) the wavefield contains increasing errors in the phase velocities and group velocities of propagating modes [Claerbout, 1970b]. Equation [7] is thus known as the  $15^\circ$  or narrow bandwidth approximation since it accurately propagates a cone of rays with a spread of about  $15^\circ$  or less.

Dropping the second derivative  $u_{rr}$  leads to greater errors for nonhorizontal raypaths [Volk, 1975] and also requires that discontinuities in acoustic properties, as at the ocean-sediment interface, must be smoothed in order to apply the method [Tappert, 1977].

Fitzgerald [1975] compared parabolic equation solutions with exact normal mode solutions. For a particular mode of order  $m$  with phase velocity  $c_m = \omega/k_m$ , and initial range  $r_0$ , Fitzgerald suggested the following limitation on the maximum distance,  $r - r_0$ , over which the parabolic equation is useful at frequency  $f$ :

$$r - r_0 \ll c_m^2 c_0 / [f(c_m - c_0)^2] . \quad [8]$$

The above equation applies to sound waves in the SOFAR channel and to RSR (refracted surface reflected) propagation. Typical limits imposed by [8] are 111 km at 100 Hz to 15,000 km at 10 Hz. For the case of bottom limited propagation, the required small finite difference step size and consequently, the long time spent computing, poses a greater practical restriction on the valid range than equation [8]. In general, the parabolic equation will be accurate to longer ranges as the frequency  $f$  decreases or  $c_m$  approaches  $c_0$ .

An implicit finite difference formulation of the parabolic equation

Following McDaniel [1975b], an implicit finite difference algorithm is constructed for equation [7]. To simplify the notation, equation [7] can be written as

$$u_{zz} = \frac{1}{a} u_r + bu, \quad [9]$$

where  $a = i/2k$ ,  $b = 2k(k_0 - k)$ , and  $k = k(z,r)$  can be complex.

Now, equation [9] is solved numerically. In the discussion that follows, the subscript  $m$  indexes steps in the  $z$  direction and the superscript  $n$  indexes steps in the  $r$  direction. A grid point has the coordinates  $(m,n)$  and the value of the wavefield at that point is  $u_m^n$ . As  $n$  is incremented, the wavefield is propagated in the  $r$  direction. At each range step  $n$ , the algorithm moves through values of  $m$  in the  $z$  direction. The first derivative in  $r$  is approximated by

$$u_r = \frac{u_m^{n+1} - u_m^n}{d_n} + O(d_n), \quad [10]$$

where  $d_n$  is the range grid spacing from  $u^n$  to  $u^{n+1}$ .  $O(d_n)$  is the approximate local truncation error at point  $(m,n)$ . Since a difference



expression such as equation [10] is derived from a Taylor series, the truncation error results from the neglected terms in the series. The second derivative in  $z$  at  $u_m^n$  is approximated by [Gerald, 1970]

$$u_{zz} = 2 \frac{u_{m+1}^n - u_m^n}{H h_m} - 2 \frac{u_m^n - u_{m-1}^n}{H h_{m-1}} + O(h) . \quad [11]$$

where  $H = (h_m + h_{m-1})$ ,  $h = H/2$ , and  $h_m$  is the depth grid spacing from  $u_m$  to  $u_{m+1}$ . When every  $h$  is the same (equispaced grid in  $z$ ), equation [11] takes on the common form

$$u_{zz} = \frac{u_{m+1}^n - 2u_m^n + u_{m-1}^n}{h^2} + O(h^2) . \quad [12]$$

Note that the error has fallen to  $O(h^2)$ .

For the moment, we shall let  $h$  be constant. The second difference operator  $\delta_z^2$  is defined as follows:

$$\delta_z^2 u_m^n = u_{m+1}^n - 2u_m^n + u_{m-1}^n . \quad [13]$$

The actual second derivative and the second difference operator have the following relation:

$$u_{zz} = \frac{\delta_z^2 u_m^n}{h^2} + O(h^2) . \quad [14]$$

From a Taylor expansion [Mitchell and Griffiths, 1980],

$$\frac{\delta_z^2 u_m^n}{h^2} = (u_{zz})_m^n + \frac{1}{12} h^2 (u_{zzzz})_m^n + O(h^4) . \quad [15]$$

Averaging derivatives between the two range steps  $n$ ,  $n+1$ , gives a form of the frequently used Crank-Nicolson equation for solving finite difference problems:

$$\frac{\delta_z^2}{2h^2} (u_m^{n+1} + u_m^n) = (u_{zz})_m^{n+1/2} + \frac{1}{12} h^2 (u_{zzzz})_m^{n+1/2} + O(h^4 + d^2) \quad [16]$$

where the field value  $u$  averaged between the two range steps  $n$ ,  $n+1$ , is

$$u_m^{n+1/2} = \frac{u_m^{n+1} + u_m^n}{2} .$$

The left side of equation [16] could more generally be written as

$$\frac{\delta_z^2}{h^2} (\theta u_m^{n+1} + (1 - \theta) u_m^n) . \quad [17]$$

In the case of equation [16],  $\theta = 1/2$ .  $\theta = 1$  yields the fully implicit formula while using  $\theta = 0$  results in the fully explicit formula. For  $1/2 \leq \theta \leq 1$ , this type of differencing scheme is unconditionally stable, even for the case of complex coefficients [Lee and Papadakis, 1979]. Hood [1978], and Claerbout [1970a] state that using a value of  $\theta$  greater than  $1/2$  may improve the accuracy of the propagated wavefield. However,  $1/2$  is a practical choice since the increased accuracy obtained by selecting another value is usually marginal when considering the computer time required to determine the optimum value.

Substituting the right side of equation [9] as a replacement for  $u_{zz}$  in the right side of equation [16] and also using equation [10] produces

$$\begin{aligned} \frac{\delta_z^2}{2h^2} (u_m^{n+1} + u_m^n) &= \frac{1}{a^{n+1/2}_d} (u_m^{n+1} - u_m^n) + (bu)_m^{n+1/2} + \\ \frac{h^2}{12d} \frac{\delta_z^2}{h^2} \left( \frac{u_m^{n+1} - u_m^n}{a^{n+1/2}_m} \right) &+ \frac{h^2}{12} \frac{\delta_z^2}{h^2} (bu)_m^{n+1/2}, \end{aligned} \quad [18]$$

$$\text{where } (bu)_m^{n+1/2} = \frac{b_m^{n+1} u_m^{n+1} + b_m^n u_m^n}{2}.$$

Now we let  $h = H/2$  and use equation [11] to define the  $\delta_z^2$  operator for a grid with variable spacing;

$$\frac{\delta_z^2 u_m}{h^2} = 2 \frac{u_{m+1} - u_m}{H h_m} - 2 \frac{u_m - u_{m-1}}{H h_{m-1}}. \quad [19]$$

The final difference equation is obtained by inserting equation [19] into equation [18] and rearranging to get equation [20];

$$\begin{aligned}
& u_{m+1}^{n+1} \left( \frac{1}{H h_m} - \frac{H}{24 d h_m a_{m+1}} - \frac{H b_{m+1}^{n+1}}{48 h_m} \right) + \\
& u_{m-1}^{n+1} \left( \frac{1}{H h_{m-1}} - \frac{H}{24 d h_{m-1} a_{m-1}} - \frac{H b_{m-1}^{n+1}}{48 h_{m-1}} \right) + \\
& u_m^{n+1} \left( \frac{-1}{H} \left( \frac{1}{h_m} + \frac{1}{h_{m-1}} \right) - \frac{1}{a_m^{n+1/2} d} - \frac{b_m^{n+1}}{2} + \right. \\
& \left. \frac{H}{24 d} \left( \frac{1}{h_m a_m} + \frac{1}{h_{m-1} a_m} \right) + \frac{H}{48} \left( \frac{b_m^{n+1}}{h_m} + \frac{b_{m-1}^{n+1}}{h_{m-1}} \right) \right) \\
= & u_{m+1}^n \left( \frac{-1}{H h_m} - \frac{H}{24 d h_m a_{m+1}} + \frac{H b_{m+1}^n}{48 h_m} \right) + \\
& u_{m-1}^n \left( \frac{-1}{H h_{m-1}} - \frac{H}{24 d h_{m-1} a_{m-1}} + \frac{H b_{m-1}^n}{48 h_{m-1}} \right) + \\
& u_m^n \left( \frac{1}{H} \left( \frac{1}{h_m} + \frac{1}{h_{m-1}} \right) - \frac{1}{a_m^{n+1/2} d} + \frac{b_m^n}{2} + \frac{H}{24 d} \left( \frac{1}{h_m a_m} + \frac{1}{h_{m-1} a_m} \right) - \right. \\
& \left. \frac{H}{48} \left( \frac{b_m^n}{h_m} + \frac{b_{m-1}^n}{h_{m-1}} \right) \right) .
\end{aligned} \tag{20}$$

The local truncation error of equation [20] is  $O(h^4 + d^2)$  when the finite difference grid is equispaced. Equation [20] may be rewritten as

$$A_{m-1}^{n+1} u_{m-1}^{n+1} + B_m^{n+1} u_m^{n+1} + C_{m+1}^{n+1} u_{m+1}^{n+1} = D_{m-1}^n u_{m-1}^n + E_m^n u_m^n + F_{m+1}^n u_{m+1}^n . \quad [21]$$

$m$  runs from 1 to  $M$  where  $M$  is the total number of grid points in the  $z$  direction. The set of equations represented by equation [21] may be written as the tridiagonal matrix equation [22];

$$\begin{bmatrix}
 B_2^{n+1} & C_3^{n+1} & & & & & \\
 A_2^{n+1} & B_3^{n+1} & C_4^{n+1} & & & & \\
 & A_3^{n+1} & B_4^{n+1} & C_5^{n+1} & & & \\
 & & \cdot & \cdot & \cdot & & \\
 & & & A_{m-4}^{n+1} & B_{m-3}^{n+1} & C_{m-2}^{n+1} & \\
 & & & & A_{m-3}^{n+1} & B_{m-2}^{n+1} & C_{m-1}^{n+1} \\
 & & & & & A_{m-2}^{n+1} & B_{m-1}^{n+1}
 \end{bmatrix}
 \times
 \begin{bmatrix}
 u_2^{n+1} \\
 u_3^{n+1} \\
 u_4^{n+1} \\
 \vdots \\
 u_{m-3}^{n+1} \\
 u_{m-2}^{n+1} \\
 u_{m-1}^{n+1}
 \end{bmatrix}
 =
 \begin{bmatrix}
 D_1^n u_1^n + E_2^n u_2^n + F_3^n u_3^n + \text{TOP} \\
 D_2^n u_2^n + E_3^n u_3^n + F_4^n u_4^n \\
 D_3^n u_3^n + E_4^n u_4^n + F_5^n u_5^n \\
 \vdots \\
 D_{m-4}^n u_{m-4}^n + E_{m-3}^n u_{m-3}^n + F_{m-2}^n u_{m-2}^n \\
 D_{m-3}^n u_{m-3}^n + E_{m-2}^n u_{m-2}^n + F_{m-1}^n u_{m-1}^n \\
 D_{m-2}^n u_{m-2}^n + E_{m-1}^n u_{m-1}^n + F_m^n u_m^n + \\
 \text{BOTTOM}
 \end{bmatrix}
 \quad [22]$$

The wave field is propagated along the  $r$  direction. For each range index  $n$ , the matrix or equation [22] must be inverted to solve for the field  $u$  at index  $n+1$ . The term "implicit finite difference" comes from the fact that the field value  $u^{n+1}$  is determined from the field at  $n$  by inverting a matrix rather than from direct multiplication. Special numerical methods are available to invert tridiagonal matrices such as the left side of equation [22] [Hornbeck, 1975].

Since  $m = 1$  corresponds to the surface of the ocean, the free surface (pressure equal to zero) boundary condition is implemented by setting  $u_1^n = 0$  and the term  $TOP = 0$  for all  $n$ . A simplified version of the Neumann boundary condition given by Lee and Papadakis [1979] is used at the very bottom of the grid. Note that, in a homogenous medium with a uniformly spaced grid and zero pressure at both surface and bottom, the left hand matrix of equation [22] is symmetric.

The accuracy of the implicit finite difference algorithm developed here was verified by computing the steady state wave field for published models [Volk, 1975; Jensen and Kuperman, 1980].

### Source modeling

The acoustic data presented in the next chapter consist of many shots recorded by one receiver. To model such data, the acoustic source is placed at the location of the original receiver. The principle of reciprocity states that propagation from the position of the receiver to each shot is the same as that for shot to receiver. The source used in the modeling is the Gaussian pulse specified by Tappert [1977];

$$\text{Source}(z, r=0) = P \exp( -(z - z_s)^2 / (2/k_0^2) ) . \quad [23]$$

$$P = p_0 i \sqrt{\pi} / ( \sqrt{2}/k_0 )$$

$$z_s = \text{source depth}$$

$$p_0 = \text{initial pressure}$$

The exact value of the source amplitude  $P$  does not matter since absolute signal levels are not modeled.

### Including attenuation in the parabolic equation

Attenuation is introduced by using a complex wavenumber,  $(k + i\alpha)$ , where  $k = \omega/c$ . The standing wave  $\exp(ikz)$  along the  $z$  axis becomes, with attenuation;

$$e^{i(k + i\alpha)z} = e^{-\alpha z} e^{ikz} . \quad [24]$$



The units of  $\alpha$  are nepers (Np) per unit length [Sheriff, 1973]. If A is the attenuation coefficient in decibels per unit length, then,

$$\alpha = \frac{A}{20 \log_{10} e} = \frac{A}{8.686} \quad [25]$$

[Clay and Medwin, 1977]. In this thesis, it is assumed that A varies linearly with frequency [Hamilton, 1972].

Attenuation expressed in terms of the intrinsic Q is [Aki and Richards, 1980]

$$\exp\left(\frac{-2\pi f z}{2 c Q}\right) = \exp(-\alpha z)$$

$$\frac{1}{Q} = \frac{\alpha c}{f} \quad [26]$$

where c is the phase velocity and f is frequency. For a 25 Hz wave traveling at 1500 m/s, an attenuation coefficient of 1.5 dB/km is equivalent to a Q of about 100.

### Modeling the ocean-sediment interface

The modeling of discontinuities such as the water-sediment interface requires special attention. Both the density and velocity contrasts across a boundary must be considered. The use of the acoustic wave equation [1] requires that the ocean bottom be modeled as fluid rather than solid material. The assumption of a fluid bottom is thought to be reasonable for many ocean acoustics problems, except when

the sediments are thin (Vidmar, 1980). In thin sediments, the P to S-wave conversions at the sediment-basement interface cause propagation loss effects that are ignored by a fluid sediment model.

McDaniel and Lee [1982] developed an implicit finite difference scheme that specifically satisfies acoustic interface boundary conditions, but the method is not readily adaptable to the case of a sloping bottom. Interfaces can be approximated by rapid, but continuous, variations in velocity and density, and that is the method used here. Replacing the wavenumber  $k$  ( $k = k(r,z)$ ) of equation [7] with  $K$  given below will include the effect of density gradients [Brekhovskikh, 1980, p. 162; Tappert, 1977].

$$K^2 = k^2 + \frac{1}{2\rho} \nabla^2 \rho - \frac{3}{4} \left( \frac{1}{\rho} \nabla \rho \right)^2 \quad [27]$$

The terms of equation [27] involving density may be neglected if the changes in density are small over a wavelength. One difficulty in using equation [27] is that  $K$  is very dependent upon the curvature of the rather arbitrary curve that one chooses to represent the density contrast at an interface. Rather than explicitly varying  $k$  through the use of equation [27],  $k$  (or  $c$ ) in the vicinity of an interface will be specified so that the theoretical reflectivity of the interface region is close to the Rayleigh reflectivity of the true acoustic interface.

The theory of Brekhovskikh [1980] was implemented to model an interface by simultaneously considering the density and velocity contrast across the interface. The interface is approximated by an Epstein layer (named after the Soviet physicist P. Epstein) with

parameters  $M$ ,  $N$ , and  $m$ . The square of the index of refraction,  $n^2(z)$ , for a horizontal Epstein layer where  $k = k(z)$  and  $c = c(z)$  is given by

$$n^2 = \left[ \frac{k}{k_1} \right]^2 = \left[ \frac{c_1}{c} \right]^2 = 1 - \frac{N \exp(m(z - z_0))}{(1 + \exp(m(z - z_0)))} - \frac{4 M \exp(m(z - z_0))}{(1 + \exp(m(z - z_0)))^2} . \quad [28]$$

$z_0$  is the Epstein layer depth ( $z$  measured positive downward),  $c_1$  is the constant velocity in the medium well above the layer, and  $k_1 = 2\pi/\lambda_1$ . The constant  $M$  depends upon the density contrast at the interface, while  $N$  is determined from the velocity contrast. A plane wave propagates in the medium above the layer and is both reflected and transmitted. In the present work, acoustic interfaces are modeled using equation [28]. Setting  $M = 0$  gives

$$n^2 = 1 - \frac{N \exp(m(z - z_0))}{(1 + \exp(m(z - z_0)))} , \quad [29]$$

which represents the square of the index of refraction due solely to a velocity contrast across the interface (Figure 1). For  $z \ll z_0$  equation [28] becomes  $n^2 = (c_1 / c)^2 = 1$ , i.e.,  $c(z) = c_1$  above the Epstein layer. For  $z \gg z_0$   $n^2 = (c_1 / c_2)^2 = 1 - N$ , where  $c_2$  is the velocity below the Epstein layer. Thus,  $N$  is determined from  $N = 1 - (c_1 / c_2)^2$ .

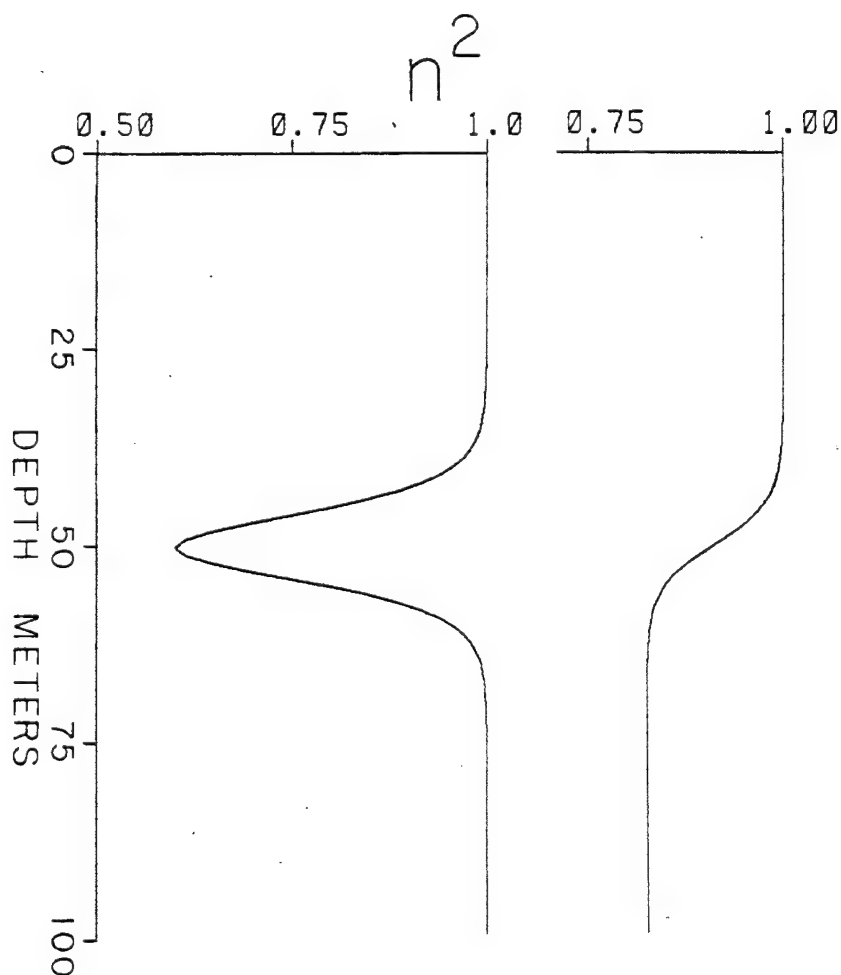


Fig. 1. Left:  $n^2$ , the index of refraction squared, for the symmetrical component (equation [30]) of the Epstein layer which describes the density contrast across an interface ( $M = 0.4$ ).

Right:  $n^2$  for the transitional component (equation [29]) of the Epstein layer which accounts for the velocity contrast across an interface ( $c_1 = 1490$  m/s,  $c_2 = 1641$  m/s). Parameters common to both figures are  $\ell = 10$  m, and  $z_0 = 50$  m.

Now, setting  $N = 0$  in equation [28] results in the equation for a density contrast only

$$n^2 = 1 - \frac{4 M \exp( m(z - z_0))}{(1 + \exp( m(z - z_0)))^2}, \quad [30]$$

which is plotted in Figure 1. Note that equation [30] is near unity except when  $z$  is near  $z_0$ , where it approaches  $1 - M$ . Morris et al. [1978] suggested iteratively changing the model velocity-depth function near the continuous interface until the model reflectivity matches the Rayleigh reflectivity of the true interface. Here, modeling interfaces proceeds along similar lines. In this case,  $M$  is varied by trial and error until the Epstein layer reflectivity matches the Rayleigh reflectivity for the interface. Thus,  $M$  is not directly specified from the known density values above and below an interface.

The term  $m$  is related to the Epstein layer thickness and may be interpreted using equation [30]. The distance between the half maximum points of equation [28] is  $\ell = 3.5254/m$ . The parameter  $S = 2k_1/m$  is called the relative thickness of the layer.  $k_1 = 2/\lambda_1$ , where  $\lambda_1$  is the incident wavelength.  $\ell$  should be smaller than  $\lambda_1$ , yet larger than the computational grid spacing.

Based upon a solution of the reduced wave equation [2], Brekhovskikh [1980, p. 171] computed the complex reflection coefficient or  $R_{pp}$  (P-wave incident, P-wave reflected), for the Epstein layer of equation [28];

$$R_{pp} = \frac{\Gamma(\gamma - 1) \Gamma(1 - \beta) \Gamma(1 + \alpha - \gamma)}{\Gamma(1 - \gamma) \Gamma(\gamma - \beta) \Gamma(\alpha)} . \quad [31]$$

$\alpha$ ,  $\beta$ , and  $\gamma$  are complex functions of the angle of incidence, wavelength of incident wave,  $m$ ,  $N$ , and  $M$  and are given in Appendix A. The  $\Gamma(\ )$  are complex gamma functions which are numerically evaluated by use of a seven-term series expansion due to Lanczos [Luke, 1969]. A Fortran program to compute the complex gamma function is provided in Appendix A.

The Rayleigh reflection coefficient for an acoustic interface where the subscript 1 indicates a property of the upper medium, 2 refers to the lower medium, and  $\theta$  is the angle of incidence, is

$$R_{pp} = \frac{X - Y}{X + Y} , \quad [32]$$

$$\text{where } X = \frac{\rho_2}{\rho_1} , \text{ and } Y = \frac{((c_1 / c_2)^2 - \sin^2 \theta)^{1/2}}{(1 - \sin^2 \theta)^{1/2}} .$$

The interface reflectivity computed from equation [32] provides the model to which the Epstein layer reflectivity is matched.

### III. MODELING PROPAGATION ON A CONTINENTAL SLOPE.

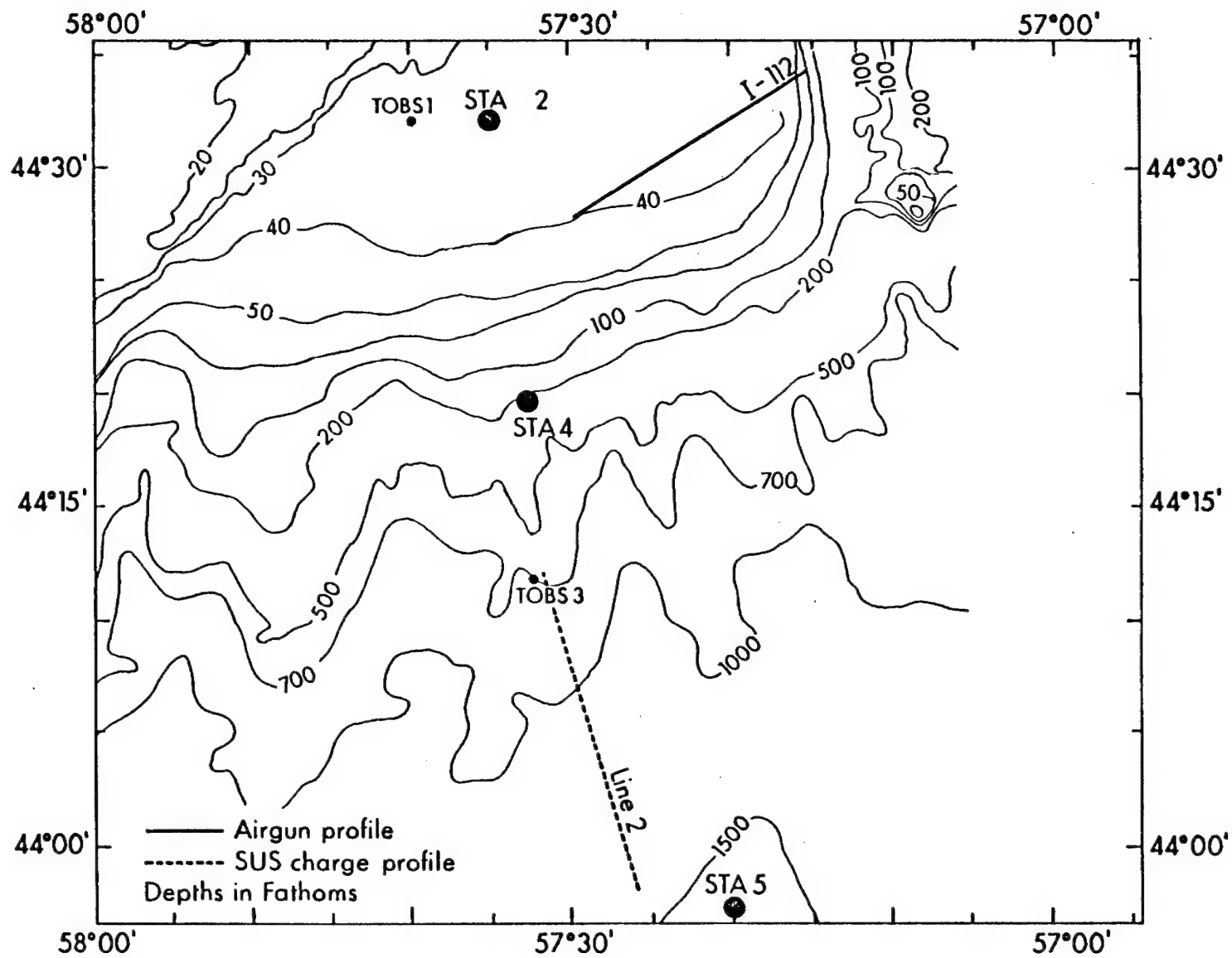
#### Field experiment

The acoustic signals modeled in this portion of the study were recorded near the edge of the continental shelf off Nova Scotia in June 1975. All signals were received by ocean bottom seismometers, each equipped with a triaxial set of geophones and a hydrophone. The instrument package, known as a TOBS (Telemetering Ocean Bottom Seismometer), has been described by Sutton et al. [1977]. In the succeeding sections, propagation loss modeling results for SUS (sound underwater signaling) explosive charges and airgun shots will be discussed. The hydrophone data was considered here since the parabolic equation calculates the acoustic pressure field for an environmental model. The hydrophone frequency response was flat from about 10 Hz to 40 Hz. Because acoustic pressure and particle velocity are linearly related [Clay and Medwin, 1976, p. 59], rates of propagation loss with range for acoustic signals measured by geophones and hydrophones should generally be identical.

The SUS charge line was situated downslope from the ocean bottom seismometer (TOBS 3) on an average slope of  $3.5^\circ$  (Figure 2). At TOBS 3 the water depth was 1301 m, while at the furthest shot, the water depth was over 2800 m. The shots were 1.1 oz (0.031kg) SUS charge boosters detonated at a depth of 18 m. Figure 2 shows the location of the SUS

Fig. 2. Location of TOBS 3 and SUS charge line on the Scotian continental slope. Velocimeter stations 4 and 5 are the sources of water velocity data for the SUS charge line. Also shown is the airgun line I-112 and receiver TOBS 1 on the shelf.





charge line on the continental slope, as well as the position of two sound velocity profiles (Figure 3).

The SUS charge arrivals are plotted in Figure 4. Also shown in the figure is the 6.4 second data window from which the propagation loss rates were calculated. The signal strength was greatest near 25 Hz, which corresponded to the bubble pulse frequency. Individual bottom bounce multiples are easily identified in Figure 4. The highest discernable group velocity was close to 1500 m/s, indicating that most of the energy propagated in the water column.

#### Physical properties of the slope

In general, acoustic modeling requires detailed environmental input because it is well known that the properties of the uppermost sediments greatly influence acoustic wave propagation in shallow water. Unfortunately, little sediment information for this SUS charge line was available. A 1.8 lb (0.82 kg) SUS charge refraction line over the same location revealed an upper sediment velocity of about 1.7 km/s [Brocher, 1982, in prep.]. Ray tracing [Appendix B] identified a bottom incident critical angle of about  $65^{\circ}$ . This result was supported by the observation of a head wave at close range resulting from incidence at  $65.2^{\circ}$  [Appendix C]. A bottom water sound speed of 1490 m/s near TOBS 3 and critical angle of  $65.2^{\circ}$  yielded an upper sediment velocity of 1641 m/s.

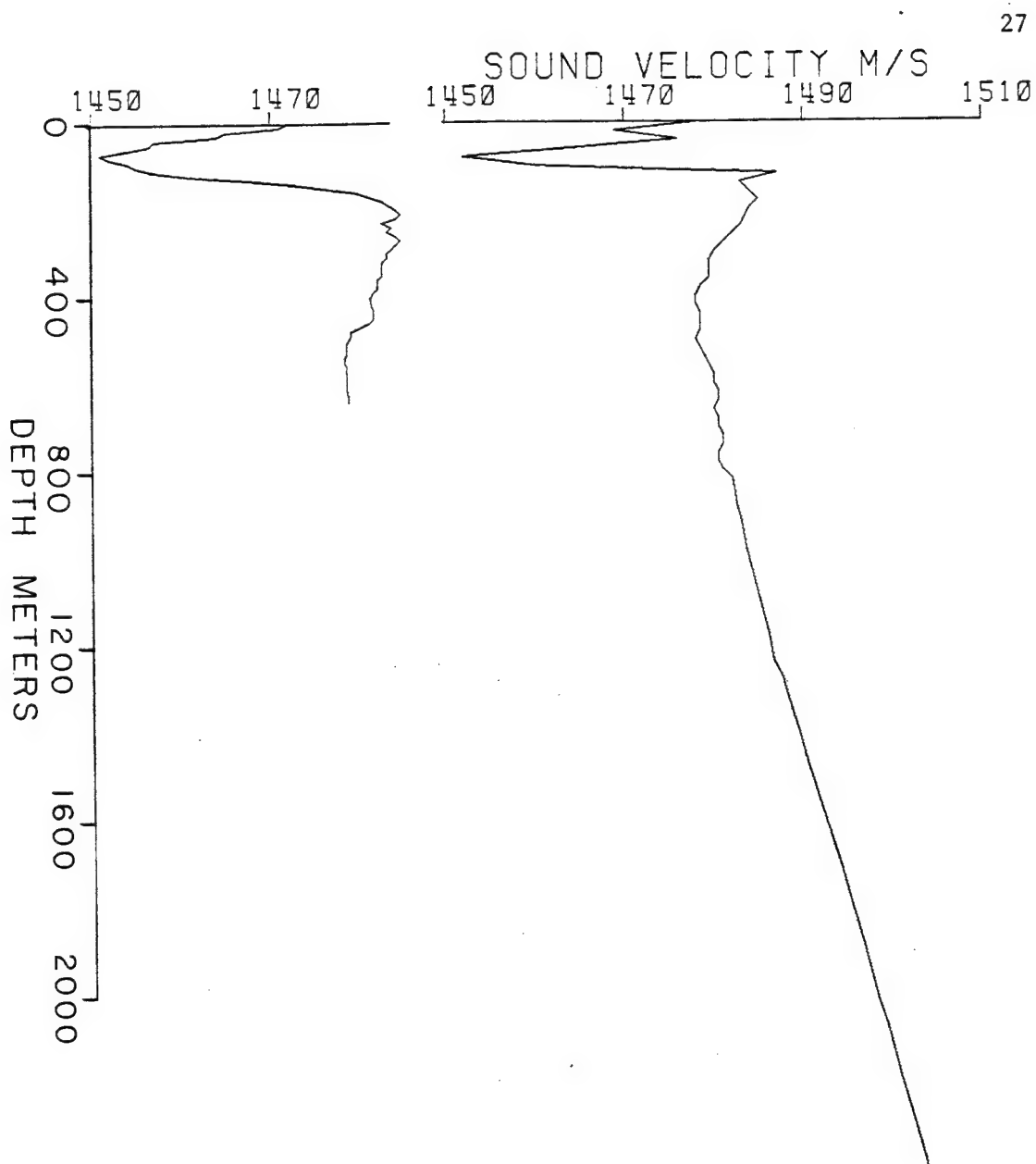


Fig. 3. Sound velocity profiles in the water column at stations 4 and 5.

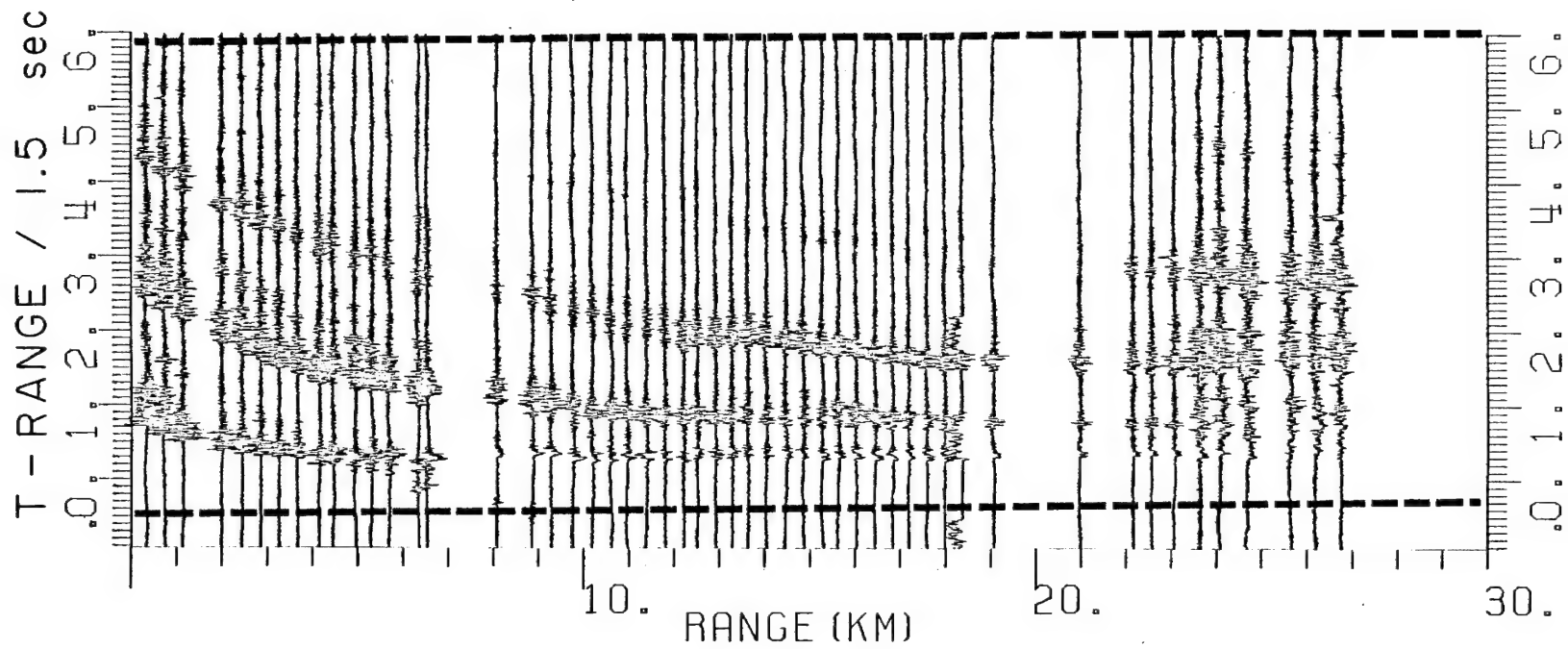


Fig. 4. SUS charge arrivals on the Scotian continental slope from shots downslope of the receiver. The dashed lines show the 6.4 second data window used for propagation loss measurement. In addition to the direct wave, three bottom multiple arrivals are observable.

Piston cores up to 13 m long from the Scotian continental slope contained muds and clays with a small percentage of sand [Piper, 1974]. The 1641 m/s mentioned above was closer to the compressional velocity in silt rather than to the lower velocity in clay [Hamilton, 1980]. The total thickness of the unconsolidated sediments was not determined. On the nearby shelf, the unconsolidated sediments were on the order of tens of meters thick, occasionally thickening to over 200 meters [Parrott et al., 1980].

#### Constructing a velocity-depth model

A velocity-depth function was obtained from the velocimeter information shown in Figure 3 and upper sediment velocities determined from the seismic refraction data. The water velocity-depth function used in the geoacoustic model was a range weighted average of data from sound velocity stations 4 and 5 between 0 and 4 km range, and was identical to the station 5 sound velocity profile beyond 4 km.

An ocean bottom sediment velocity of 1641 m/s was selected, based on the critical angle estimate. A sonic velocity gradient of  $1 \text{ s}^{-1}$  was chosen for the sediments. This gradient lies within the range of values reported for silt clays and turbidites [Hamilton, 1979]. The sediment thickness was arbitrarily set at 60 m. As a result of using this sediment velocity and thickness, and a bottom water velocity of 1492 m/s

(measured about 7 km downslope of TOBS 3), the minimum bottom incidence angle for long range propagation was  $61.3^\circ$ . That is, rays with a bottom incidence of  $61.3^\circ$  or more remained in the water column either by reaching a turning point within the upper 60 m of sediment or by postcritical reflection at the sediment-water interface. In the model, bottom incident rays at angles less than  $61.3^\circ$  were unable to turn back upwards within the upper 60 m of sediment and were lost from the sound channel.

A special provision was made for rays refracted from the sound channel into the bottom of the sediment. Although it might be preferable to follow Clayton and Engquist [1977], in which absorbing boundary conditions were used to allow waves to pass out of the computational grid without any reflection or backscatter, it is nontrivial to apply the Clayton and Engquist boundary condition on a slope. In this case the waves passing through the bottom of the sediments were simply damped out as was done by Tappert [1977]. More specifically, for every other depth grid point below the sediment layer, the attenuation was doubled while the velocity was remained constant. This doubling continued until the final attenuation was  $2^{11}$  times the attenuation in the sediments. Since the wavefield was damped out by the time it reached the bottom of the computational grid, the boundary condition at the very bottom did not matter, as long as it was physically realizable. The Neuman boundary condition on a slope was specified.

A sediment density of  $1.6 \text{ g/cm}^3$  and an attenuation in the sediments of  $1.5 \text{ dB/km}$  at  $25 \text{ Hz}$  were selected for use in the model from values computed by Beebe and McDaniel [1980] for the Scotian shelf. Beebe and McDaniel used sediment grain size data and the Biot-Stoll sediment model [Stoll, 1974] to compute the attenuation. These parameters are approximate, since it was likely that the Scotian shelf sediments had a higher sand content than those on the Scotian slope. Figure 5 summarizes the environmental parameters used in the model.

#### An Epstein layer for the water-sediment interface

The ability of ray tracing in a medium with a hard bottom to qualitatively predict variations in signal level [Appendix B] suggested that the water-sediment interface was the principal bottom reflector and consequently a deeper acoustic basement, if any, did not significantly affect the guided wave propagation in the water. Therefore, the only bottom reflector included in this parabolic equation model was the ocean bottom. As described earlier, the ocean bottom was simulated by an Epstein layer.

Figure 5 shows the geoacoustic model and the Epstein layer approximation to the ocean bottom interface. An Epstein layer half-thickness  $\ell = 10 \text{ m}$  was chosen. This choice was subject to the constraints that it be greater than the computational grid size of  $2 \text{ m}$

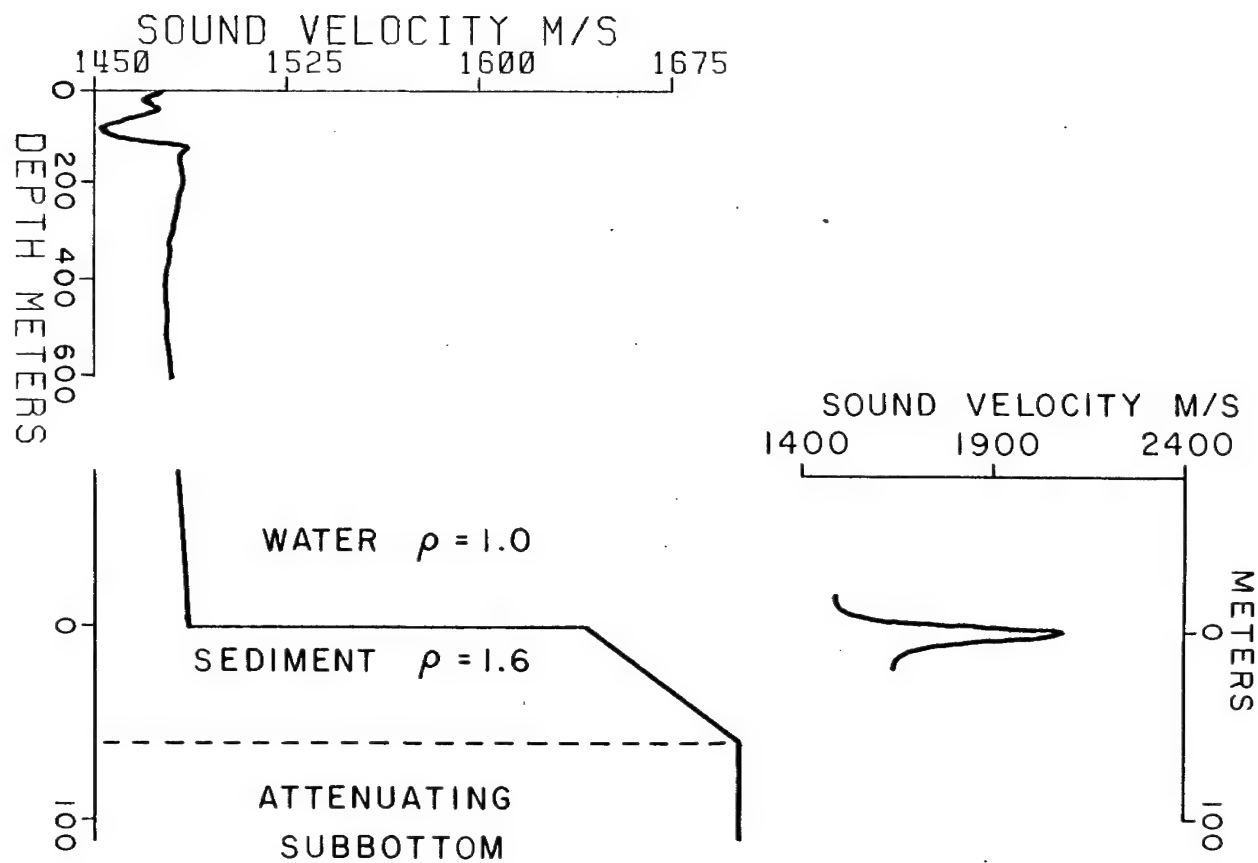


Fig. 5. Left: Geoacoustic parameters for modeling propagation on the Scotian slope.  
 Right: The equivalent Epstein layer model of the ocean bottom interface.



in the  $z$  direction, and less than the average wavelength of 60.8 m computed from a 25 Hz wave traveling with an average group velocity of 1520 m/s. Once  $\ell$  (or small  $m$ ) was selected, this left the parameter  $M$ , associated with the density contrast, as the only free variable for matching the Epstein layer reflectivity [32] to the Rayleigh reflectivity [34]. The Rayleigh and Epstein reflectivities calculated from the parameters shown in Figure 5 are compared in Figure 6. The choice  $M = 0.4$  was based upon trial and error matching of the magnitudes of the respective reflection coefficients. Note that while the magnitude of the reflection coefficient was reasonably well matched, there was a considerable mismatch in phase (Figure 6).

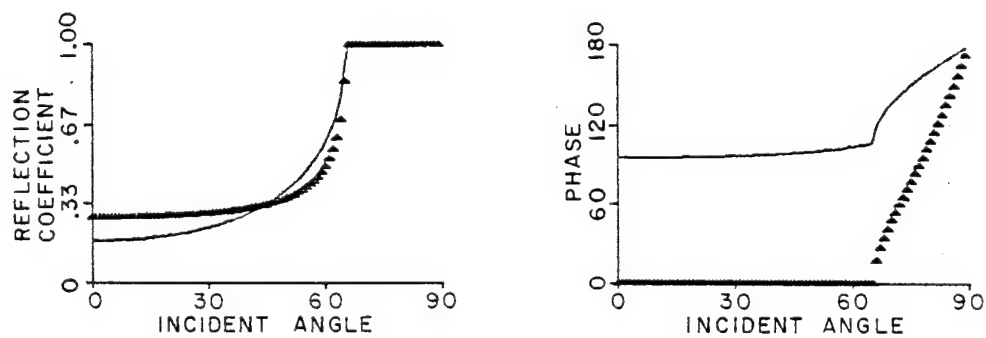


Fig. 6. Rayleigh reflection coefficient and phase ( $\Delta$ ) for the ocean bottom of Figure 5. Solid line shows the 25 Hz reflectivity for the Epstein layer model of the bottom interface.

### Choosing a computational grid

Brock [1978] described a numerical algorithm for the parabolic equation which automatically picked the range increment and  $z$  increment as the computation proceeded. However, the algorithm was based upon a Fourier transform solution of the wave equation and uniform  $z$  increment at each range step and was not directly applicable to this study. In the present analysis, the computational grid was arbitrarily chosen using the following criteria:

- i) There must be several grid points per wavelength of the propagating waves.
- ii) The grid increment must be smaller than the "wavelength" of the boundaries as well as of the source.

Both of the above requirements are restatements of the fact that the grid step size must be small enough to prevent spatial aliasing.

Table 1 lists the specifications for a fixed and variable step size grid on which the model described in Figure 5 was computed. The results for both grids are compared in the next section. The relative grid spacings are illustrated in Figure 7.

It is necessary to specify a small depth increment near the ocean bottom. In a rectangular grid, this small increment in depth persists to all ranges. With a sloping bottom, the result is a fine grid where

Table 1. -- Finite difference grid spacings for modeling propagation on the continental slope near Nova Scotia.

Grid Spacing in the Depth Direction

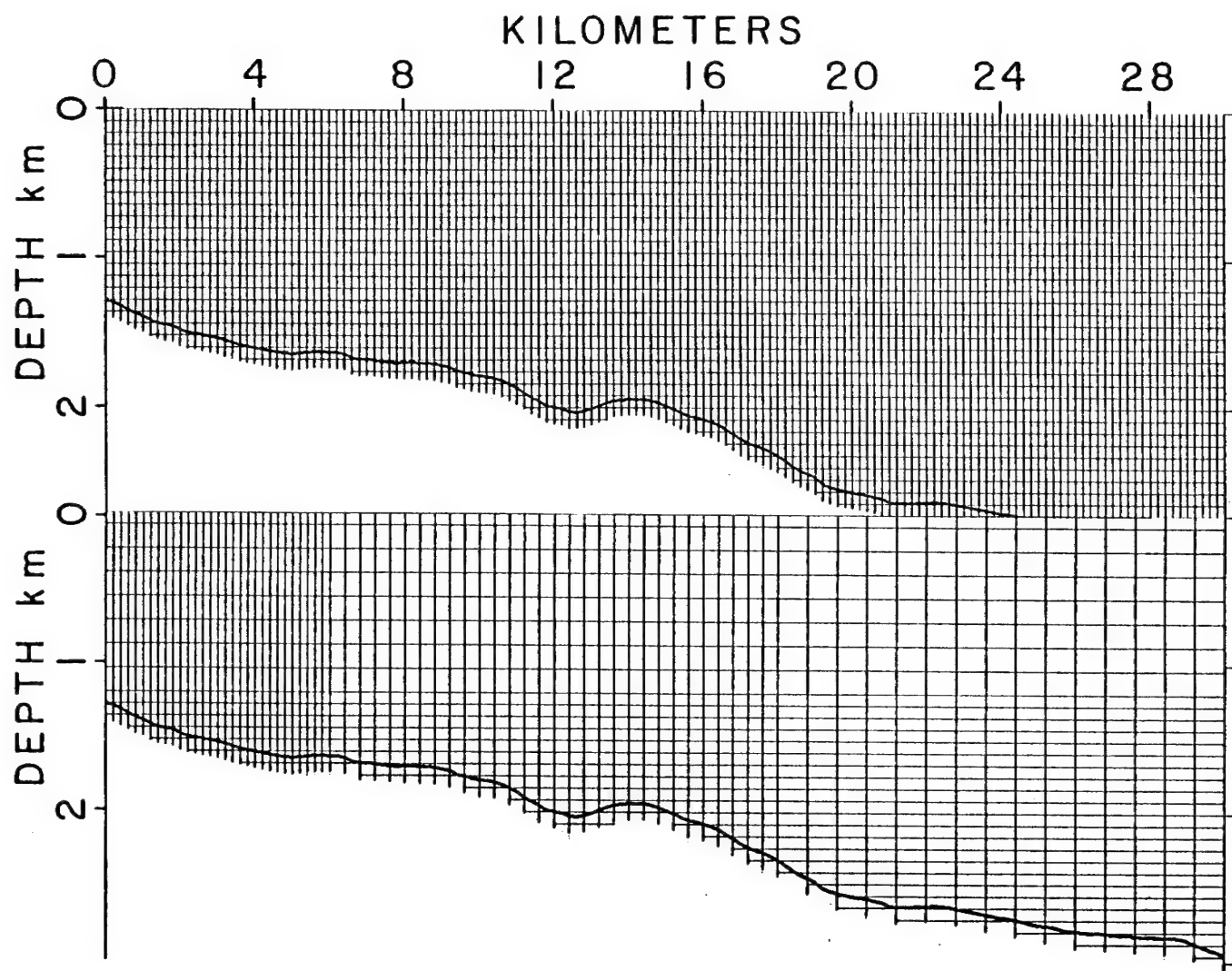
<u>Index</u>	<u>Depth, meters</u>	<u>Grid Spacing <math>\Delta z</math>, meters</u>
1	0	2
50	98	
51	100	4
320	1176	
321	1180	2
1200	2938	

Grid Spacing in the Range Direction

<u>Index</u>	<u>Range, meters</u>	<u>Grid spacing <math>\Delta r</math>, meters</u>
1	0	5
1200	5995	
1201	6000	10
2400	17990	
2401	18000	20
2919	28360	

$\Delta z = 2$  meters and  $\Delta r = 5$  meters for the constant spacing grid.

Fig. 7. Above: Constant grid spacing model.  
Below: Variable grid spacing. For both grids only about 1 in 40 grid intersections in both range and depth direction are plotted. Note that the grid length in the z direction varies with the bathymetry. The complete grid specifications are listed in Table 1.



it is not needed and increased computational costs. There are alternatives to the rectangular variable-spacing grid used in this thesis. If the slope is fairly uniform, as in the present case, effecting a non-rectangular grid which conforms to the average bottom slope saves computer time without loss of accuracy. Another possibility is to change the finite difference grid at a specified range. At that range, propagation is halted and the wave field is interpolated onto a new  $z$  grid. Computing the wave field would then proceed until it is necessary to change the grid again.

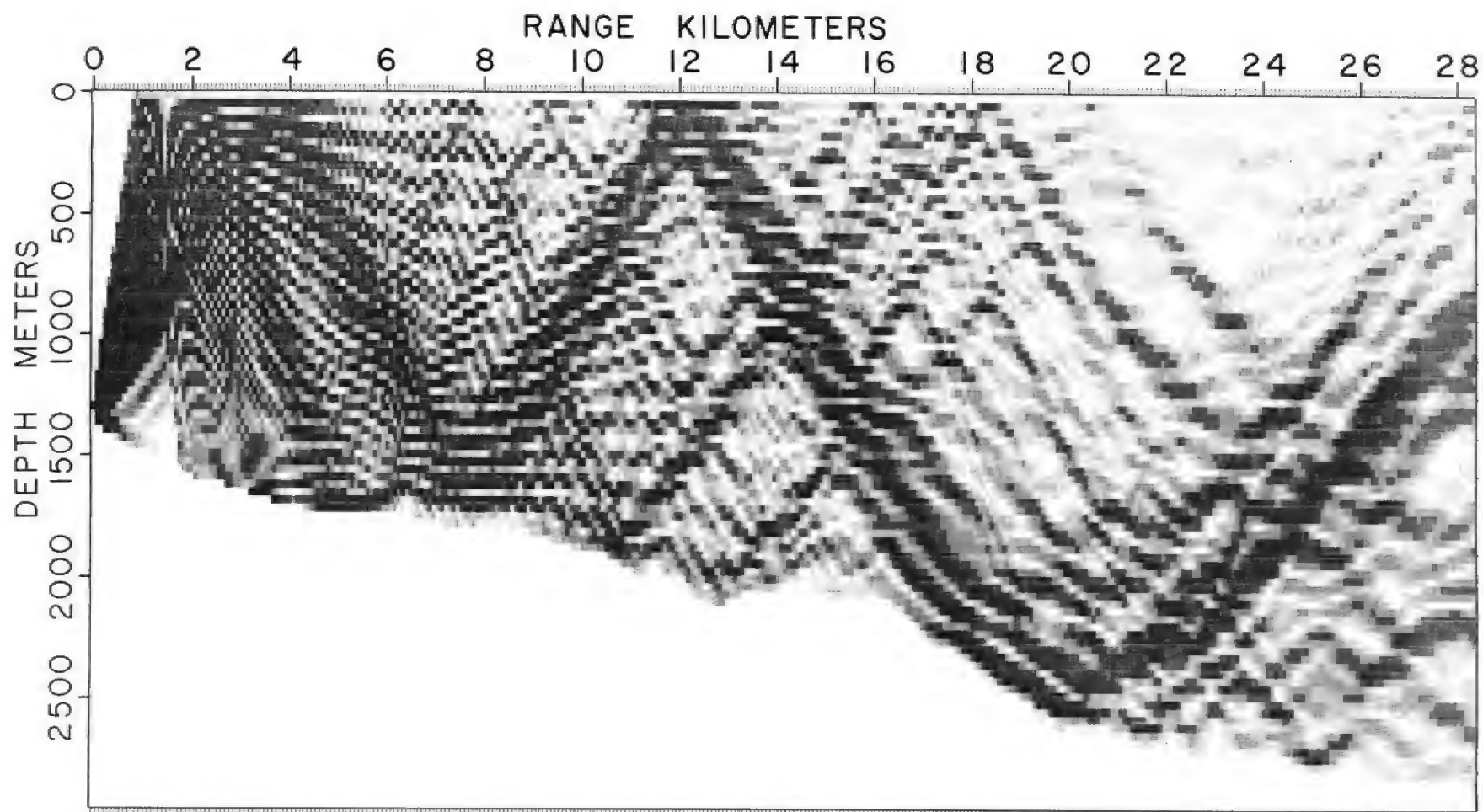
### The parabolic equation model output

Figure 8 shows the intensity of the acoustic wave field for 25 Hz generated by the parabolic equation model based on Figure 5 and the fixed grid spacing detailed in Table 1. A  $c_0$  value of 1520 m/s was used in the computation. In both the range and depth directions, the values of the wavefield at about 1 in 16 computational grid points were plotted. At short ranges, the acoustic intensity was highly oscillatory due to the propagation of many modes associated with different wave numbers (or differing phase velocities). With increasing distance, precritical reflections were quickly damped out, leaving the postcritical phases indicated by the ray traces of Figures 17-19.

Figure 9 (bottom) is a plot of the wavefield of Figure 8 at 18 m depth, the same depth as the SUS charge detonation. A least square fit straight line from 6 to 28 km yielded a propagation loss rate (negative of the slope) of 0.61 dB/km. This value was automatically corrected for cylindrical spreading because of the assumption (equation [3]) made during the derivation of the parabolic approximation. The propagation loss for the same model computed using the variable grid spacing of Table I was 0.60 dB/km (Figure 10). Figure 10 compares the variable and fixed grid computations at 18 m depth. A close examination of Figure 10 revealed only minor differences, which tended to increase with range, between the outputs of the two grids. The variable grid spacing was more economical since computing the same wavefield as in Figure 8 took



Fig. 8. Intensity of 25 Hz parabolic equation wave field. Input is the model of Figure 5 computed on the constant spacing grid. White is the weakest amplitude and black is the strongest. From black to white inclusive there are seven shades each separated by 2.6 dB. The Gaussian pulse source is seen at far left.



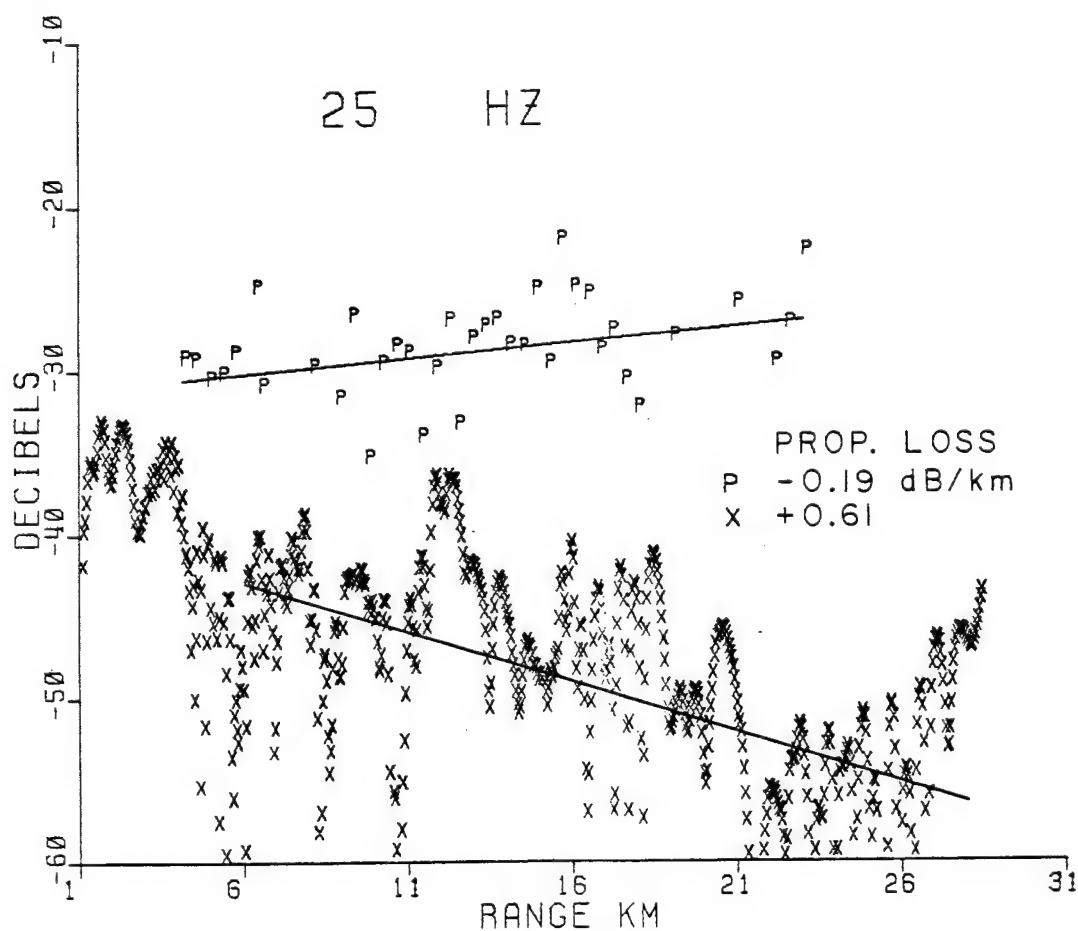


Fig. 9. Top: Observed 25 Hz SUS charge signal level versus range computed using the 6.4 second data window shown in Figure 4. The decibel values have been corrected for cylindrical spreading. The -0.19 dB/km propagation loss or negative slope is computed for ranges from 4 to 23 km.

Bottom: Computed parabolic equation wavefield at 25 Hz using the constant grid spacing of Table 1. This plot is a slice taken at 18 m depth from Figure 8. The +0.61 dB/km propagation loss is measured for ranges from 6 to 28 km.

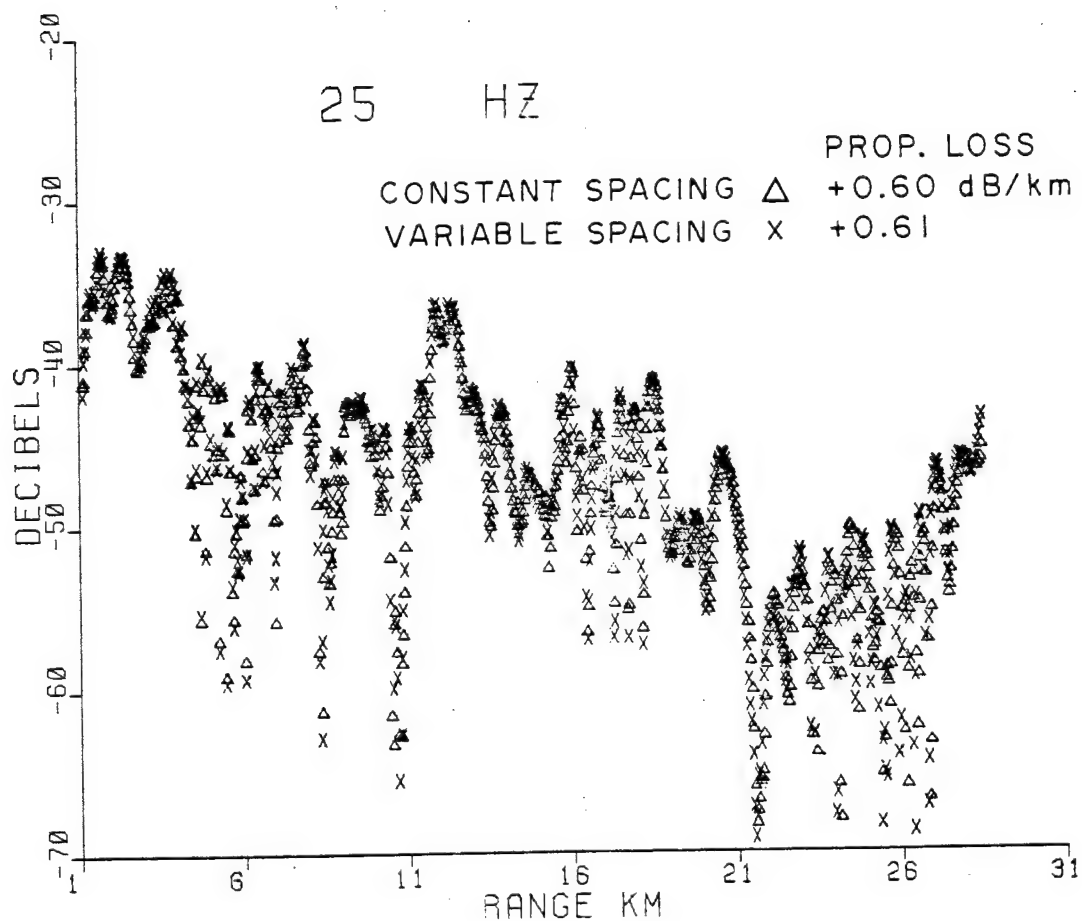


Fig. 10. Comparison of the outputs of the parabolic equation model at 25 Hz for the variable and constant grid spacing listed in Table 1 and illustrated in Figure 7. The measured +0.60 dB/km propagation loss from 6 to 28 km computed using variable grid spacing is almost the same as the +0.61 dB/km loss for the constant grid spacing case.

only 33 minutes of computing on a Harris 800 computer and required smaller arrays than the fixed grid calculation which lasted 96 minutes.

#### Comparison of the observed and predicted propagation loss

The predicted 0.61 dB/km propagation loss at 25 Hz does not match the observed negative propagation loss of -0.19 dB/km (Figure 9). It was not known why the signal level increased with range after normalizing for cylindrical spreading loss. A possible problem was that the instrumentation compressed the hydrophone signals, so that the apparent propagation loss was less than expected for cylindrical spreading.

Comparing the observed signal levels in Figure 9 with the parabolic equation predictions in the same figure showed possible common peaks at 6.5, 9.5, 16, and 23 km. In general, the shot spacing was too coarse to enable resolution of sudden changes in signal level. Significant arrivals predicted at 11.5 to 12.5 km and 16.5 to 18.5 km were absent from the data. Errors in the geoacoustic model and in modeling the source, as well as the signal compression, may explain the discrepancy between data and model.

#### IV. MODELING DATA FROM A CONTINENTAL SHELF

##### Bathymetry

Airgun profiling by an oil company vessel provided signals along a line (I-112) oblique to TOBS 1 (Figure 2). This data set provided the opportunity to analyze sound propagation in shallow water over a slope of less than 0.1 degrees. In addition, the data were of good quality and the shot coverage was dense enough to resolve sharp signal fluctuations over distances of a few hundred meters. The bathymetry along the airgun line is plotted in Figure 11. Because of the rapidly increasing water depth past 29.5 km only data at ranges less than 29.5 km were used. The water depth varied from about 90 m at 31.6 km to 83 m at a range of 10.3 km. As Figure 2 indicates, the bathymetry between the shot locations and TOBS 1 was three dimensional.

To model the bathymetry, the ocean bottom for ranges between 0 and 25.4 km was approximated by a linear increase in depth from 67 to 70 m. For ranges from 20 km to the nearest shot at 10.3 km, this model bathymetry was an inaccurate representation of the actual water depth beneath each shot. The largest error was a difference of 15 m at 10.3 km range. Nonetheless, the bathymetry model provided a good representation of the water depth for travel paths between the receiver and most shots.

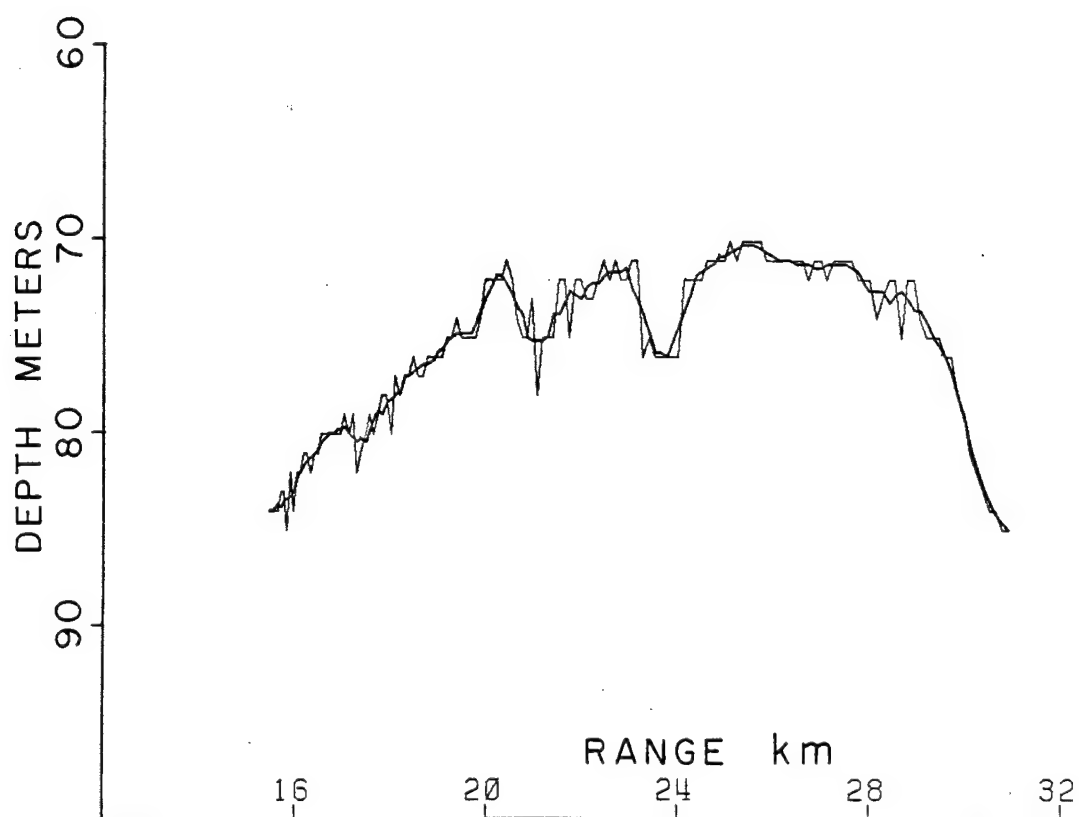


Fig. 11. Bathymetry beneath airgun shot points.

### Constructing a velocity-depth model

The unconsolidated sediments in the vicinity of Banquereau Bank are glacial and littoral deposits [Maclean and King, 1971; Parrott et al., 1980]. The surficial unit, Sable Island Sand and Gravel, is generally no more than 20 m thick [Parrot et al., 1980]. Over much of the shelf the Sable Island Sand and Gravel is underlain by the Emerald Silt and a glacial till known as Scotian Shelf Drift. Both of these units vary in thickness from a few meters to over a hundred meters. Bedrock is mostly Tertiary sandstones and shales called the Banquereau Formation [Jansa and Wade, 1974].

The recorded airgun signals are shown in Figure 12. Most of the energy in the arrivals was concentrated between 10 and 40 Hz - the peak frequency response of the hydrophone. A calculation based on the apparent velocities of the direct and trailing edge of the water wave arrivals [Houtz, 1980] [Appendix D] yielded an upper sediment velocity of 1.53 km/s. Measurements by McKay and McKay [1982] using a deep-towed device on the adjacent Sable Island Bank found upper sediment velocities from 1.57 to 1.66 km/s. The sediment velocity used in the model was 1.6 km/s.

Using a Biot-Stoll sediment model [Stoll, 1974], Beebe and McDaniel [1980] calculated a sediment attenuation of 1.5 dB/km at 25 Hz ( $Q=100$ ) for various locations on the Scotian shelf. If the exponential attenuation coefficient varies linearly with frequency then the 10 Hz



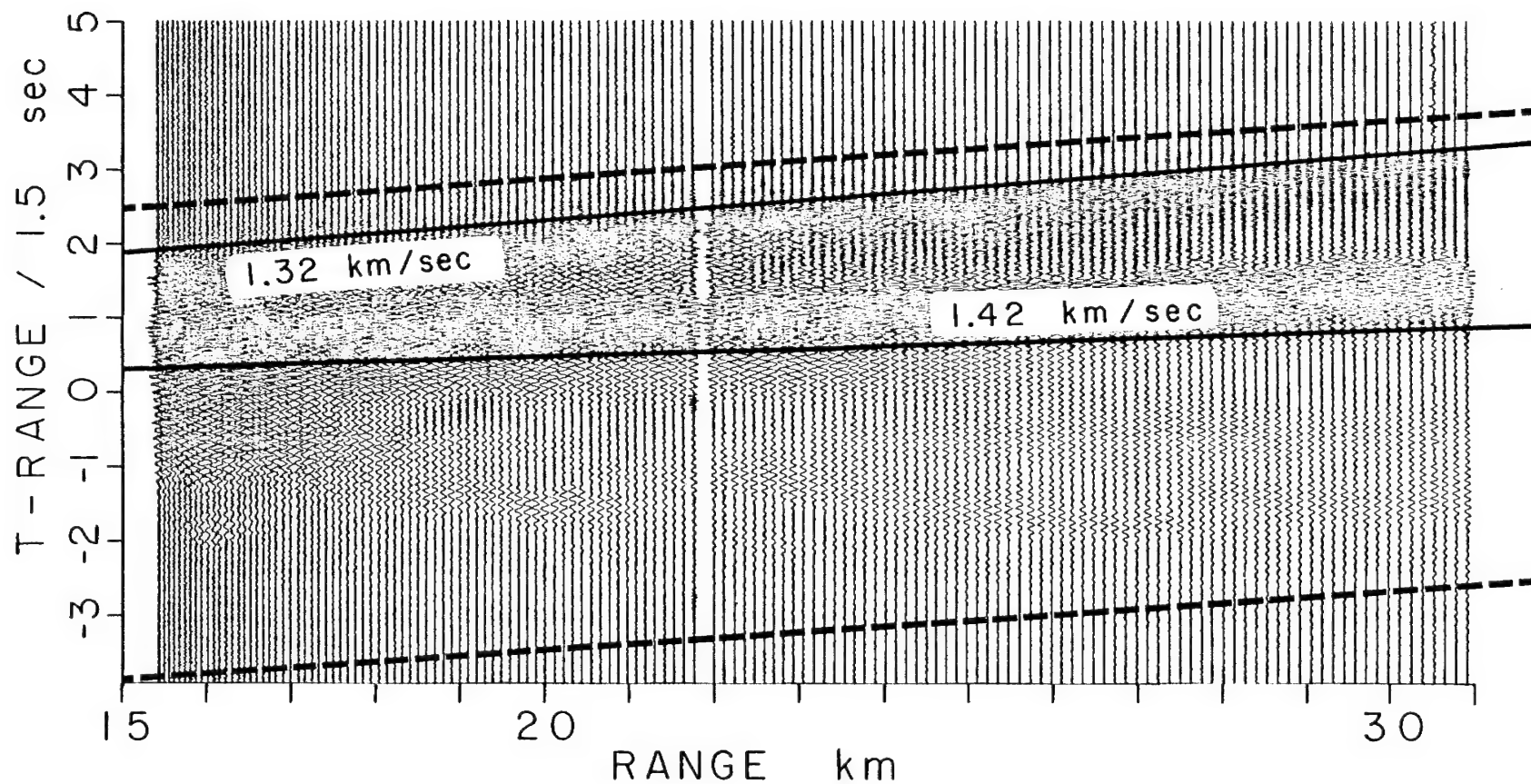


Fig. 12. Airgun data from the Scotian shelf. The dashed lines show the 6.4 second data window from which the signal level is obtained. Also indicated are the leading and trailing edges of the water wave. The 10 Hz signals preceding the water wave result from the interaction of the water wave with the subbottom. They may be reflected refractions.

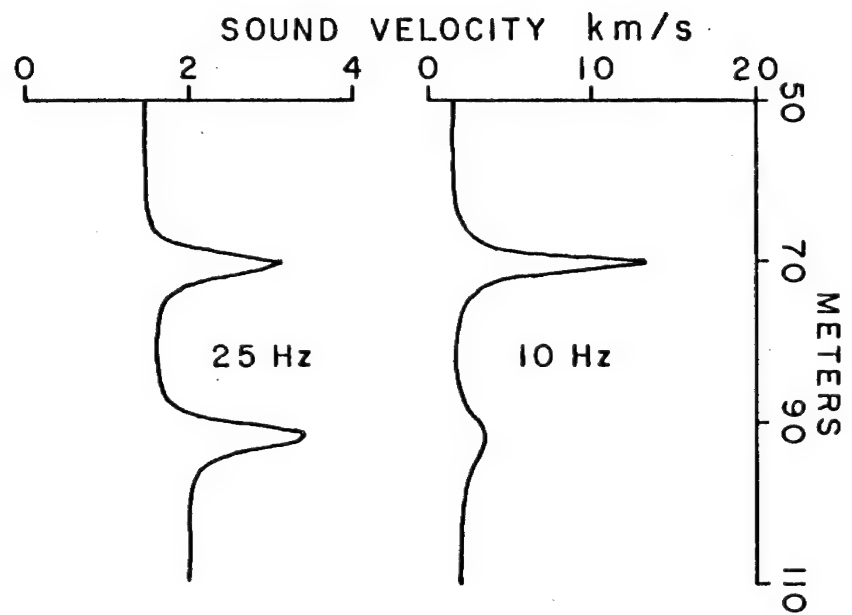
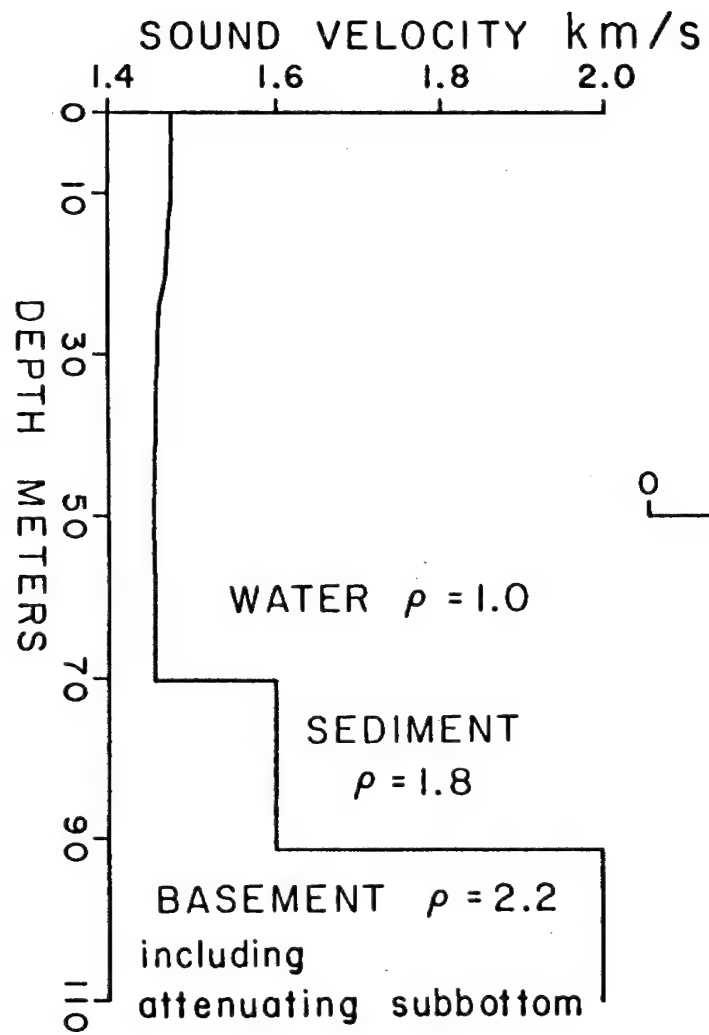
attenuation is 0.6 dB/km. The bottom density of  $1.8 \text{ g/cm}^3$  shown in Figure 13 was taken from the silty sand value given by Hamilton [1980]. The acoustic basement on the shelf was modeled using the parameters of Beebe and McDaniel [1980] which were a velocity of 2.00 km/s and a density of  $2.2 \text{ g/cm}^3$ .

The acoustic model for propagation on the shelf contained two interfaces - one at the ocean bottom and one at the acoustic basement. The model parameters are illustrated in Figure 13. Also shown in this figure are Epstein layer models of these interfaces at 25 and 10 Hz. Based on an analysis of surface wave dispersion [Brocher, 1982, in prep.], an unconsolidated sediment thickness of 21 m was used.

The 25 Hz reflectivity functions of the Epstein layer equivalents to the ocean bottom and acoustic basement interfaces of Figure 13 are plotted in Figure 14. As discussed earlier, the parameters of the Epstein layer were chosen by a trial and error matching of the Epstein reflectivity curve to the Rayleigh reflectivity curve calculated from the velocity and density contrast across the interface. The 10 Hz Epstein layer reflectivity plots for the same interfaces are shown in Figure 14 (lower). At 10 Hz it was necessary to use a 10 m Epstein layer half-thickness compared to 5 m at 25 Hz in order to adequately represent the acoustic interfaces. Thus, the extent of each 10 Hz Epstein layer was 20 m which is about the same as the model sediment thickness. Since the interfaces at the top and bottom of the sediment were modeled at 10 Hz by Epstein layers which were as thick as the 21 m

Fig. 13. Geoacoustic model for the airgun shot line on the Scotian shelf. There is an acoustic interface on the ocean bottom and at the bottom of the sediment. Waves propagating below the subbottom interface are completely damped out.

Right: Epstein layer approximations to the two interfaces at 25 and 10 Hz.



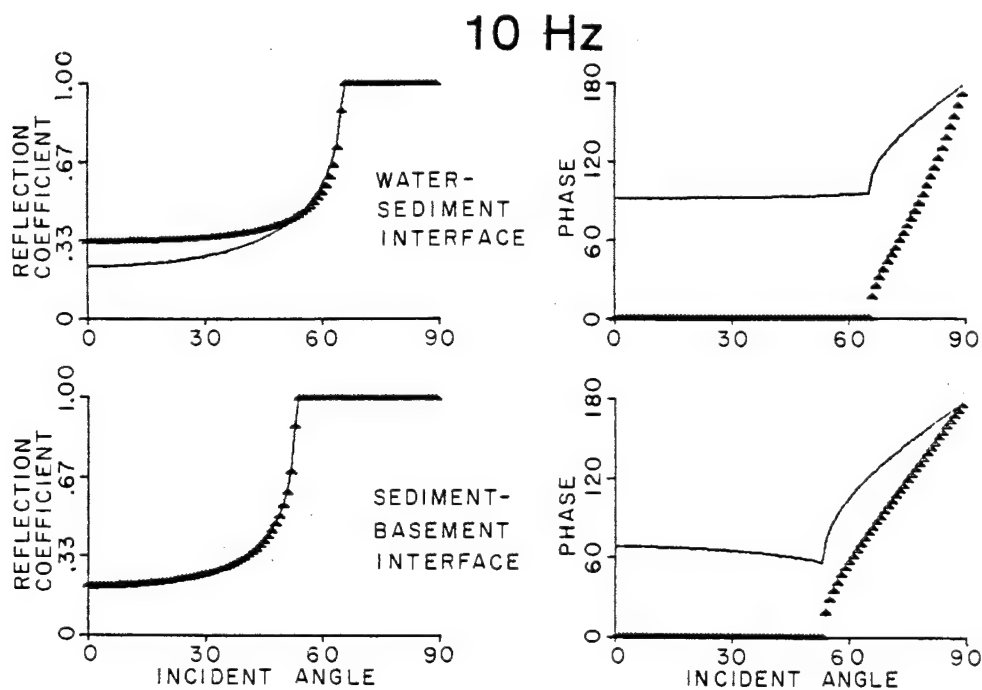
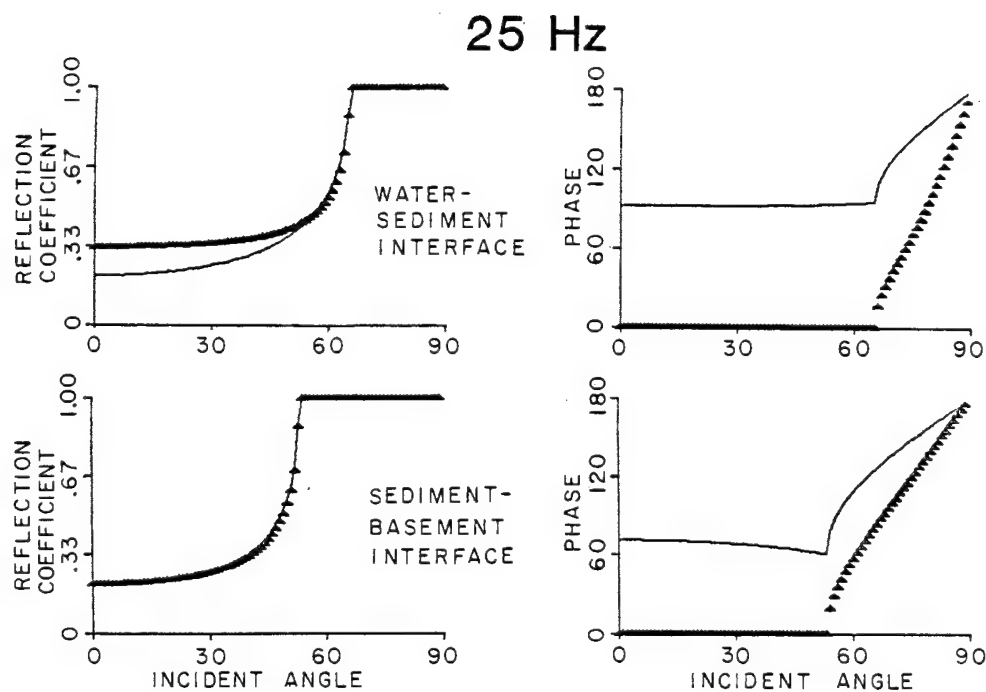


Fig. 14. Above: Rayleigh ( $\Delta$ ) and Epstein layer (solid line) reflectivities at 25 Hz for the ocean bottom (upper) and sub-bottom (lower) interfaces. The left column shows the magnitude of  $R_{pp}$ , the right column shows the phase.

Below: Same for 10 Hz

sediment layer, the 10 Hz modeling results must be taken with caution.

A sediment velocity gradient was not used because of the thinness of the unconsolidated sediment layer. The water velocity was taken from velocimeter data near TOBS 1. For the computations a  $c_0$  value of 1.46 km/s was used. The finite difference grid parameters are given in Table 2. The range increments for computing the parabolic equation wavefield were the same as for the variable grid spacing of Table 1. Smaller depth increments were used for this model because of the shallowness of the water and the need for both bottom and sub-bottom interfaces. As before, waves propagating below the sediment layer were damped out by increasing the attenuation with depth while holding the velocity constant.

#### Comparison of data to model at 25 Hz

The signal levels at 25 Hz calculated from the 6.4 second data window of Figure 12 are plotted in Figure 15 (top). The observed propagation loss rate from 15.4 to 29.5 km was -0.17 dB/km. For ranges less than 25 km the signal had a higher variance which is probably caused by the presence of a number of propagating modes at short range. Because of the shallow water, most of these modes rapidly decayed. Only the first mode could propagate beyond 25 km.

Table 2. -- Finite difference grid spacings for modeling propagation on the Scotian shelf.

Grid Spacing in the Depth Direction

<u>Index</u>	<u>Depth, meters</u>	<u>Grid Spacing <math>\Delta z</math>, meters</u>
1	0	2
62	61	
63	62	0.5
186	123.5	
187	124	1
197	134	
198	135	2
208	155	
209	157	4
234	257	

The grid spacing in the range direction is the same as in Table 1 except that the region where  $\Delta r = 20$  m is extended to 31.6 km.

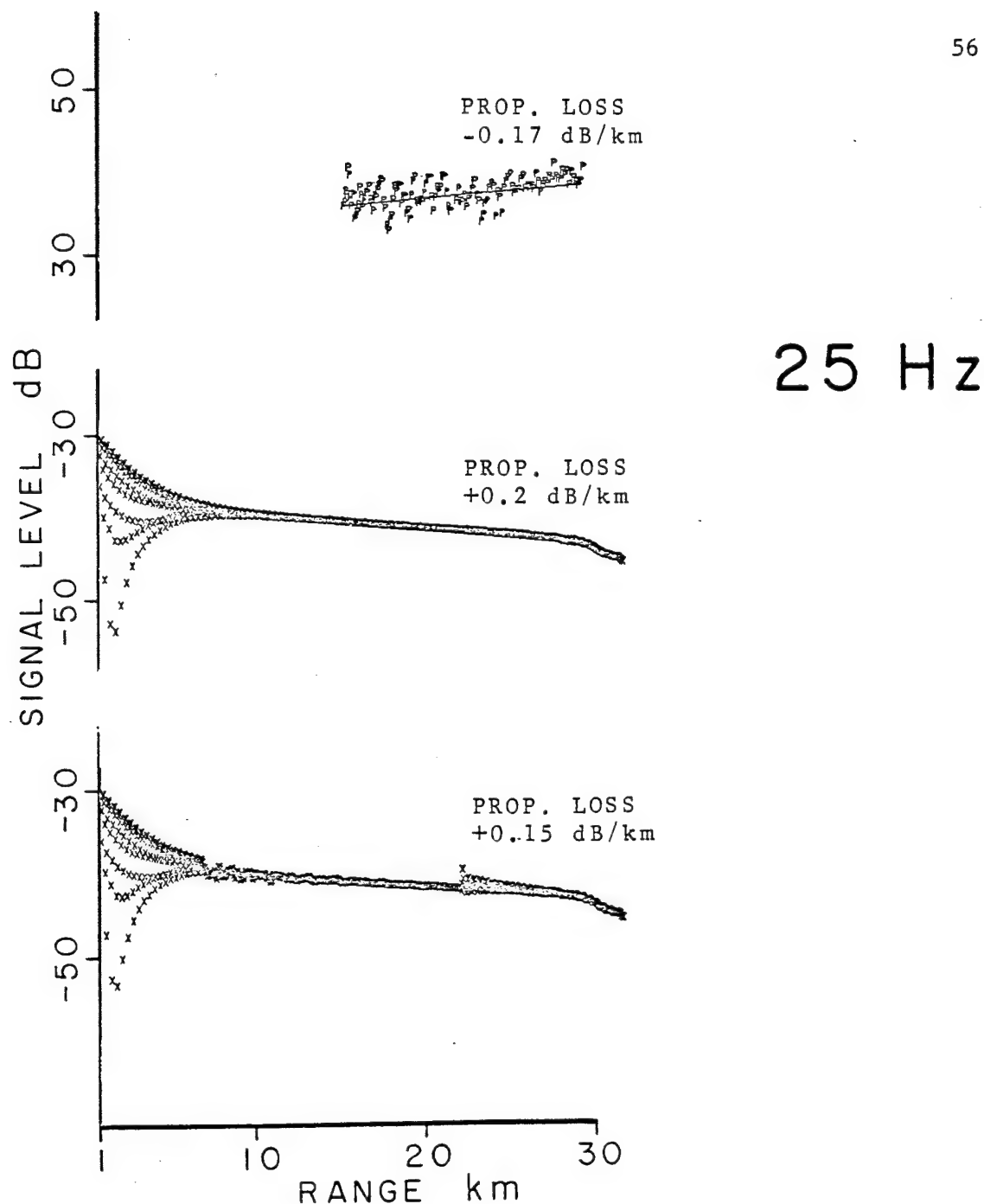


Fig. 15. Top: Observed 25 Hz airgun signal level versus range found using the 6.4 second data window shown in Figure 12. The plot is corrected for cylindrical spreading.  
 Middle: 25 Hz parabolic equation output at 9 m water depth for the acoustic model of Figure 13.  
 Bottom: Parabolic equation output for same model as used above with the addition of a 200 m thick sediment trough situated between 7 and 22 km range.



It was believed that the airgun operated at 9 m water depth. Using the model of Figure 13, the acoustic wave field at 9 m depth was calculated for 25 Hz (Figure 15, middle). The result of the calculation showed fluctuating signal levels near the source which indicated the presence of several propagating modes. The smoothness of the curve beyond a range of 10 km suggested that only one mode existed in this region. The calculated propagation loss between 15.4 and 29.5 km was 0.20 dB/km.

In both the observed data and the computed signal levels there was a transition from multimode to single mode propagation. However, the range where this transition occurred was different in both cases. This range mismatch was probably due to the use of an attenuating sub-bottom, a point which is discussed later.

In an effort to better fit the measured propagation loss rate, a 200 m thick sediment trough was added to the model between 7 and 22 km. A sediment trough could represent a model for a sediment filled Pleistocene valley or stream bed [King and MacLean, 1970]. The computed propagation loss for this model is shown in Figure 15 (bottom). The trough extended the range of multimode propagation as shown by the wiggleness at the left end of the trough, but did not provide a better fit to the data.

A sediment velocity gradient of  $1 \text{ s}^{-1}$  added to the above sediment trough model produced an insignificant change in the propagation loss results. The finding that a velocity gradient in the sediments did not

influence the propagation loss indicated that most of the energy at 25 Hz was trapped in the water column.

#### Comparison of data to model at 10 Hz

The 10 Hz spectrum level versus range is plotted in Figure 16 (top). Values for ranges between 15.4 and 27.5 km are displayed and the propagation loss was 0.14 dB/km compared to the -0.17 dB/km loss found at 25 Hz. At 10 Hz there was less variation in signal level from shot to shot than at 25 Hz.

Figure 16 also shows the calculated wavefield at 10 Hz and at a depth of 9 m in the water column plotted versus range. The calculated propagation loss between 15.4 and 27.5 km of -0.43 dB/km does not fit the data. The possibility that this propagation loss rate is controlled by the sediment column is suggested by the observation that at 10 Hz, signals propagating at 1460 m/s have a wavelength of 146 m which is twice the average water depth of about 70 m and greater than the combined water and sediment thickness of 91 m. In this case, the first mode was slightly below the cutoff frequency and the calculated signal level rapidly decayed within the first 10 km (Figure 16). Note that for a 70 m water layer with velocity 1452 m/s over a sediment half-space with velocity 1600 m/s, the cutoff frequency is 12.3 Hz. The presence of the 2000 m/s acoustic basement lowers this cutoff frequency slightly. The model sediment layer was thin in comparison with the acoustic

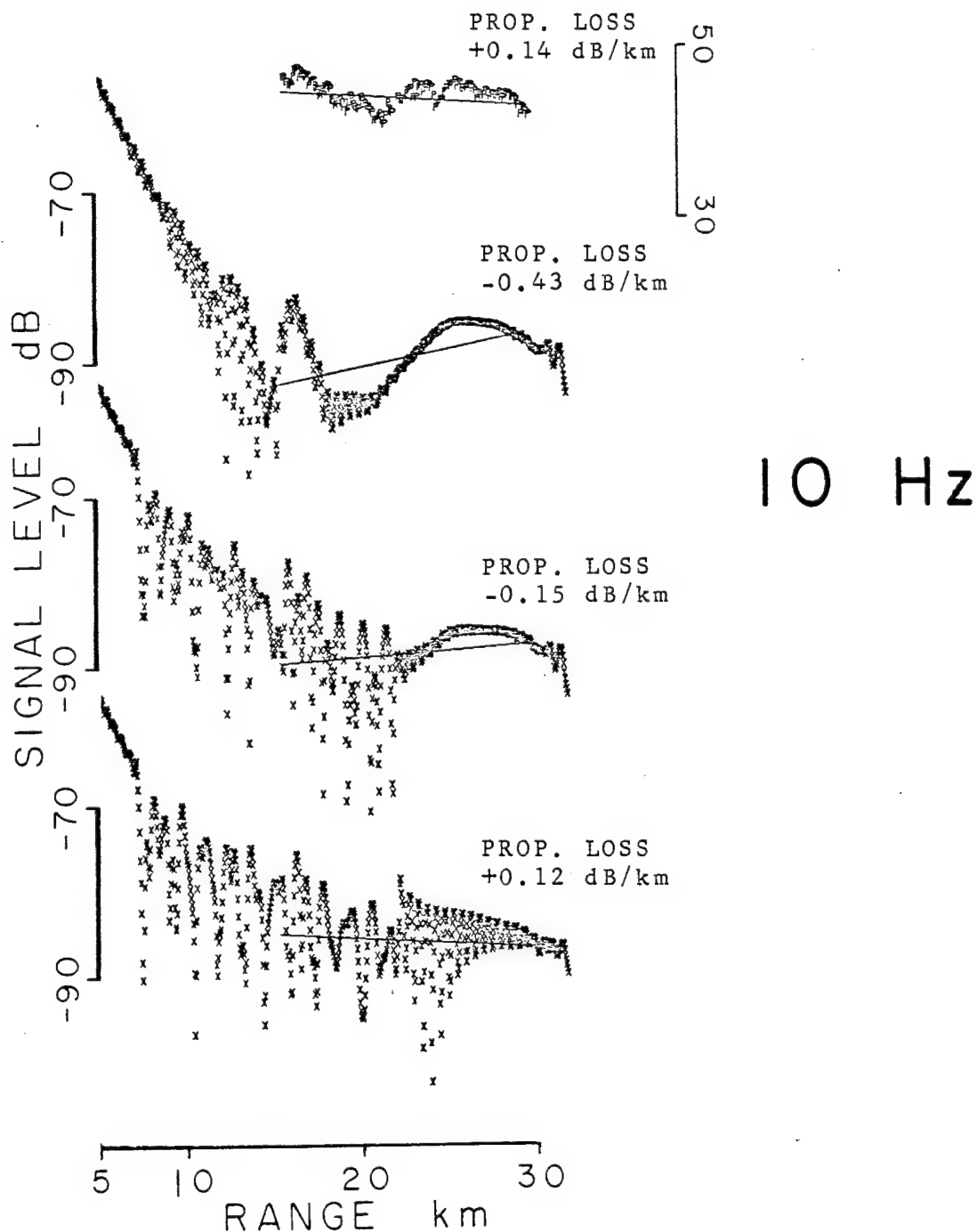


Fig. 16. From top to bottom:  
 10 Hz signal levels found using a 6.4 second window and corrected for cylindrical spreading;  
 Parabolic equation output for the geoacoustic model shown in Figure 13 at 10 Hz;  
 10 Hz output for above model with 200 m thick sediment trough from 7 to 22 km range;  
 10 Hz output for sediment trough model with  $1 \text{ s}^{-1}$  velocity gradient.

wavelength, and possible shear conversions at the sediment-basement interface [Vidmar, 1980] which cause additional propagation loss were neglected by the parabolic equation used here.

Adding the 200 m thick sediment trough between 7 and 22 km gave a propagation loss of -0.15 dB/km (Figure 16). Placing a  $1 \text{ s}^{-1}$  gradient in the sediment trough model resulted in a realistic propagation loss of 0.12 dB/km (Figure 16, bottom) but the variance in the model signal level was much greater than that of the data. It was obvious that, as a consequence of the shallowness of the water with respect to the 10 Hz wavelength, the sediments controlled the propagation loss rate.

## V. DISCUSSION ON SOURCES OF MODELING ERROR

In the acoustic modeling presented here, several approximations were made which deserve attention as likely sources of error. The parabolic equation is limited to treating a narrow band of propagating rays. The Epstein layer is an approximation to the acoustic interface and causes a phase error in the reflected wavefield. Applying the Gaussian source pulse at an interface may cause errors. The use of an attenuating sub-bottom is not physically real and may affect propagation loss. These four factors are discussed below.

Earlier it was mentioned that equation [7] is known as the  $15^\circ$  or narrow bandwidth approximation. In the model for propagation on the Nova Scotian continental slope, the critical angle at the water-sediment interface was  $65.2^\circ$ . Coincidentally, the same angle was obtained for critical incidence at the water-sediment interface in the Scotian shelf model. Since most of the propagating modes of the computed wave fields were associated with postcritical bottom reflections, the incidence angles associated with those modes ranged from  $65^\circ$  to  $90^\circ$ . This spread of  $25^\circ$  was thus greater than the  $15^\circ$  limit of equation [7]. In general, the error arising from using the  $15^\circ$  approximation to propagate a wider range of incident rays or corresponding phase velocities causes a shift in the positions of convergence zones [Brock et al., 1977].

The phases of the Epstein layer and Rayleigh reflection coefficients were quite different, as is shown in Figures 6 and 14. This phase difference was unavoidable since the Epstein layer "reflects"

rays by forcing them to turn. Since the wave field computed from equation [7] is a standing wave interference pattern, the incorrect phase caused by using Epstein layers can be expected to cause significant shifts in the position of local field values. Choosing the Epstein layer parameters so that the magnitude of the Epstein layer reflection coefficient matched that of the Rayleigh interface, however, ensured that the energy trapped in the water layer was identical to that when acoustic interfaces are included in the modeling. Thus, one would expect the propagation loss rates found over long distances to be similar for models employing Epstein layers and models using true interfaces.

There is also some inaccuracy introduced by placing the Gaussian pulse on the water-sediment interface. The Gaussian source pulse [23] was selected from a variety of possible source functions because it is simple to compute. An alternative would be to use as initial data the normal mode wavefield at a short range from the source [Wood and Papadakis, 1980]. It seems probable that the symmetric source function [23] did not accurately model the source on the interface. The water-sediment interface itself was modeled as a smoothly varying transition zone. Placing a Gaussian pulse on such a transition region should at least be more physically reasonable than locating the pulse on a discontinuity.

The use of an attenuating sub-bottom causes higher order modes associated with rays at precritical bottom incidence to be prematurely damped out. This result may be seen in Figure 15 by comparing the

observed and predicted 25 Hz signal levels. The higher order modes in the observed signal level are present out to about 25 km. In the predicted signal levels, the higher order modes are not visible beyond 12 km. In this example, improper modeling of the bathymetry and sediment properties may also be responsible for the premature decay of the higher modes. However, it is likely that, at close ranges, use of an attenuating sub-bottom causes erroneous propagation loss when precritical bottom reflections are significant.

## VI. SUMMARY

An implicit finite difference algorithm for the parabolic equation based on a variable grid spacing in the depth as well as range direction was developed. The algorithm, when implemented with a variable grid spacing, gave almost the same results as a constant fine grid spacing in one third as much computer time.

Acoustic interfaces, characterized by a velocity and a density contrast, were modeled by using Epstein layers. The Epstein layer parameters were selected by fitting the amplitude of the theoretical Epstein layer reflectivity [Brekhovshkikh, 1980] to the acoustic Rayleigh reflectivity. The use of Epstein layers provided an interface-like aspect to the acoustic models. It was necessary, however, to specify Epstein layer thicknesses roughly proportional to the acoustic wavelength, making the Epstein layer difficult to use for low frequency modeling of interfaces separated by a thin layer.

Propagation loss curves were computed using this algorithm for shot lines on the Scotian slope and shelf. The modeling results were compared with data recorded by hydrophones positioned on the ocean bottom. On the Scotian slope, the observed  $-0.19$  dB/km propagation loss at 25 Hz could not be replicated. The observed negative propagation loss may be partly caused by compression of the signals by the recording instrumentation.



On the Scotian shelf, in water about 70 m deep, the modeling could not explain the observed  $-0.17$  dB/km propagation loss at 25 Hz. At this frequency, the sub-bottom acoustic parameters did not greatly effect the modeled propagation loss. This result was in agreement with the observation that 25 Hz was well above the cutoff frequency for normal mode propagation in the water column. On the other hand, 10 Hz was close to the cutoff frequency and the observed  $0.14$  dB/km propagation loss at 10 Hz was simulated by adjusting the properties of the sediments. Seismic reflection profiling on the slope and shelf would be helpful for determining the depth to acoustic basement and extent of lateral sediment changes needed to improve the geoacoustic models.

# APPENDIX A. EPSTEIN LAYER REFLECTIVITY FUNCTION

The parameters of equation [31] are here described in detail.  $S = 2k_1/m$  is the relative thickness of the Epstein layer.  $\theta$  is the angle of incidence of the plane wave upon the Epstein layer.  $M$  is the constant of equation [28] which is related to the density contrast across the interface for which the Epstein layer is an approximation.  $N$  is the constant that is determined by the velocity contrast across the interface.  $\alpha$ ,  $\beta$ , and  $\gamma$  of equation [31] are specified by the following equations:

$$A = \operatorname{Re} \left[ \frac{1}{2} (1 - 4S^2 M)^{1/2} \right]$$

$$B = \operatorname{Im} \left[ \frac{1}{2} (1 - 4S^2 M)^{1/2} \right]$$

$$\alpha = \frac{1}{2} + A + (iS/2) [\cos \theta - (\cos^2 \theta - N)^{1/2}] + iB$$

$$\beta = \frac{1}{2} + A + (iS/2) [\cos \theta + (\cos^2 \theta - N)^{1/2}] + iB$$

$$\gamma = 1 + iS \cos \theta$$

Brekhovskikh [1980] derived the above expressions by relating the solution of the reduced wave equation [2] to the solution of the hypergeometric equation.

The Fortran program given on the next page computes  $\Gamma(z+1)$  for  $\text{Re}(z) > -11/2$ . For values of  $z$  outside this range, continuation formulas may be used. Here a seven term series expansion due to Lanczos is implemented (Luke, 1980). A typical error for  $\ln \Gamma(z)$  is on the order of  $10^{-7}$ . If  $z = x + iy$ , then  $e^z = e^x(\cos(y) + i\sin(y))$ . This relation may be used if complex exponentiation is not provided on the user's computer.

```

1:      FUNCTION CGAM(CZ)
2: C    CGAM IS THE GAMMA FUNCTION FOR COMPLEX ARGUMENT Z
3: C    FOR INPUT COMPLEX Z, OUTPUT IS GAMMA(Z + 1).
4: C
5: C    REQUIRE REAL(Z) > -11/2
6: C    HOWEVER, IT IS STRONGLY RECOMMENDED THAT YOU USE CONTINUATION
7: C    FORMULAS FOR REAL(Z) < 0 BECAUSE OF THE SINGULARITIES IN
8: C    GAMMA(Z+1) WHEN Z = -1, -2, -3, ETC.
9: C
10: C    THIS IS THE LANCZOS EXPANSION FROM
11: C    Y.L. LUKE, THE SPECIAL FUNCTIONS AND THEIR APPLICATIONS,
12: C    ACADEMIC, N.Y., 1969, VOL. 1 & 2.
13:      IMPLICIT COMPLEX(C)
14:      DIMENSION G(0:6)
15: C    THERE ARE (NORD + 1) G CONSTANTS
16: 5      NORD = 6
17:      G(0) = 41.624436916439068
18:      G(1) = -51.224241022374774
19:      G(2) = 11.338755813488977
20:      G(3) = -0.747732687772388
21:      G(4) = 0.008782877493061
22:      G(5) = -0.000001899030264
23:      G(6) = 0.000000001946335
24:      PI = 3.141592654
25:      E = 2.718281828
26:      PI2SQ = SQRT(2.0 * PI)
27:      C11 = CZ + 11.0 / 2.0
28:      C2 = CZ + 0.5
29:      C2 = C11 ** C2 * PI2SQ
30:      C2 = C2 * E ** (C11 * (-1.0))
31:      CH = (1.0,0.0)
32: 10     CSUM = (0.0,0.0)
33:      FOR I = 0, NORD
34:      .   CSUM = CSUM + CH * G(I)
35:      .   RIX = I
36:      .   RIX1 = I + 1
37: 20     .   CH = CH * (CZ - RIX) / (CZ + RIX1)
38:      END FOR
39:      CGAM = C2 * CSUM
40:      RETURN
41:      END

```

## APPENDIX B. RAYTRACING ON THE CONTINENTAL SLOPE

This appendix describes raytrace modeling of acoustic signals recorded on the continental slope off Nova Scotia. The modeled signals are the same as those modeled using the parabolic equation as described in Chapter 2. The SUS charge line was downslope from the telemetering ocean bottom seismometer (TOBS 3) on an average slope of  $3.5^\circ$ . At TOBS 3 the water depth was 1301 m, while at the furthest shot the water depth was over 2800 m. The shots were 1.1 oz (0.031 kg) SUS charges detonated at a depth of 18 m. Figure 2 shows the location of the SUS charge line on the continental slope, as well as the position of two sonic velocity versus depth profiles of the water column (Figure 3).

For this shot line the water was sufficiently deep to allow individual bottom bounce multiple arrivals of the water wave to be readily identified. Yet, the ocean was shallow enough so that beyond a few km range, the most energetic arrivals were all reflections off the bottom. In addition, the average  $3.5^\circ$  slope (local slopes were as much as  $18^\circ$ ) caused the angle of incidence of a downslope-propagating ray to increase upon each bottom bounce; the incidence angle of an upslope-propagating ray would have decreased.

Ray tracing is a useful tool for this problem because it enables the observer to visualize actual wave propagation effects. Water wave arrivals recorded by TOBS 3 and the ray traces for one, two, and three bottom multiple arrivals are pictured in Figures 17 to 19. In these ray trace figures, the rays emanate from the position of TOBS 3 in 0.5

degree increments. A composite of sonic velocity stations 4 and 5 is used for the water velocity versus depth function. The bottom reflects all incident rays and is slightly smoothed to eliminate errant rays caused by irregularities in the bathymetry profile.

For single bottom bounce water wave arrivals (Figure 17), the shape of the ocean bottom is the most significant factor affecting propagation loss. A convex bottom near 9 km creates a small shadow zone at 15 km range while a convex bottom near 14 km results in a shadow zone from 24 to 30 km (up to the limit of the plot). A concave bottom near 13 km range produces a region of high intensity between 17 and 18 km which shows up in the data between 16 and 17 km range. This discrepancy is probably caused by slight errors in modeling the bathymetry and water column velocity. Another possible source of error is neglect of azimuthal dependence in the raytracing.

The two and three bottom bounce multiple arrivals indicated in Figures 18 and 19 largely consist of postcritical reflections since suffering more than one precritical reflection greatly reduces the amplitude of the arrival. Beyond 13 km surface range, the increased amplitude of the second multiple (Figure 18) is due to the second bounce reaching or exceeding critical incidence of about  $65^\circ$  (incident angles are measured from the normal to the bottom), starting from around 9.5 km range on the bottom. For this discussion, bottom bounces are counted from the first bounce downslope of the ray source on the bottom. Between 13 and 18 km range, the second bounce arrival is additionally intensified by bottom focusing.

Careful examination reveals some increase in the amplitude of the third multiple arrivals (Figure 19) between 14 and 16 km, due to bottom focusing. However, only past 22 km do the third multiples become significant, a consequence of their becoming critically incident at these ranges. The family of post critical third bounce arrivals after 22 km originates from the second multiples seen between 13 and 18 km.

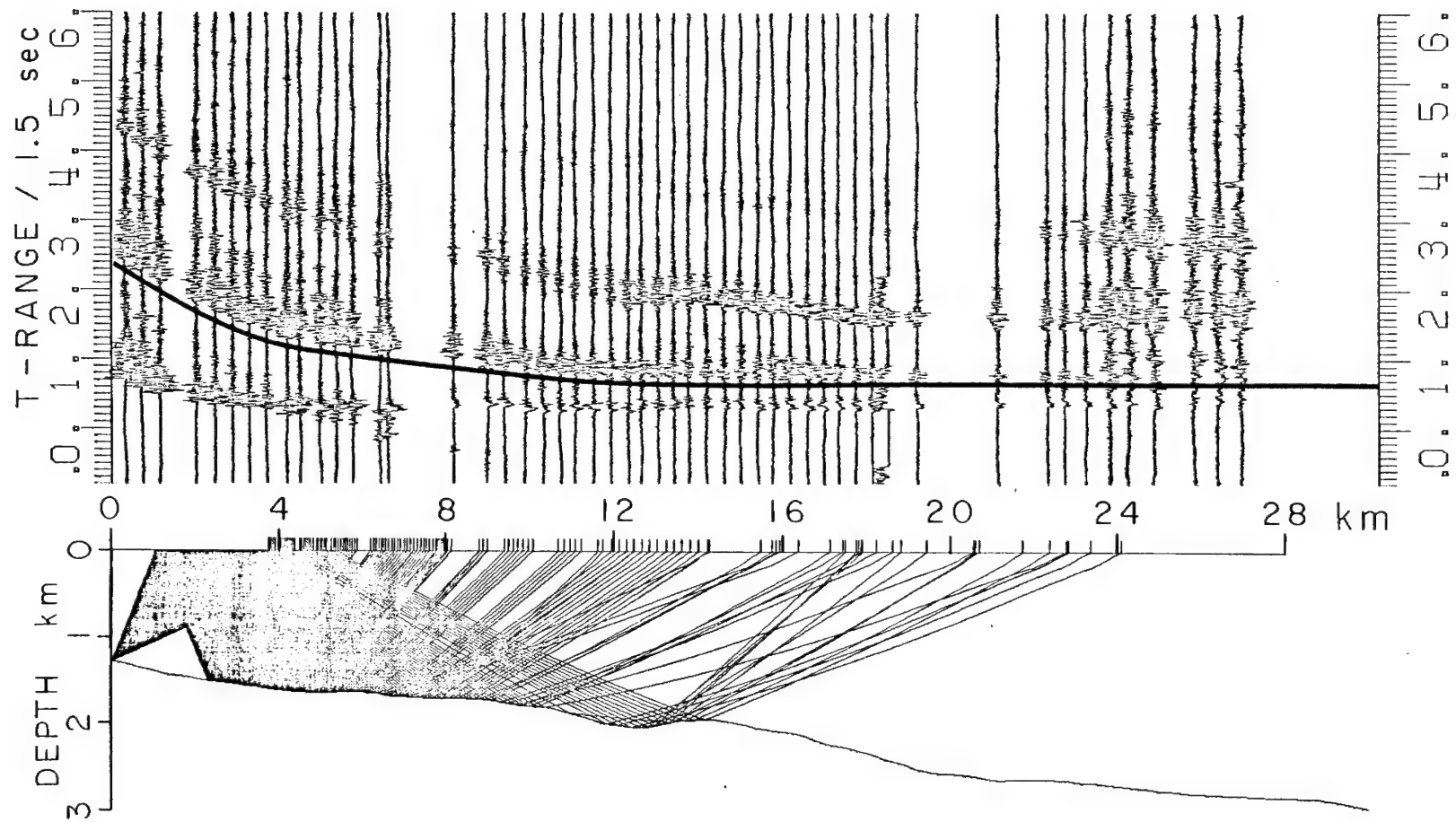


Fig. 17. One bottom bounce ray paths from TOBS 3. The shape of the ocean floor creates a shadow zone beyond 24 km. The solid line precedes the single bottom bounce arrivals.



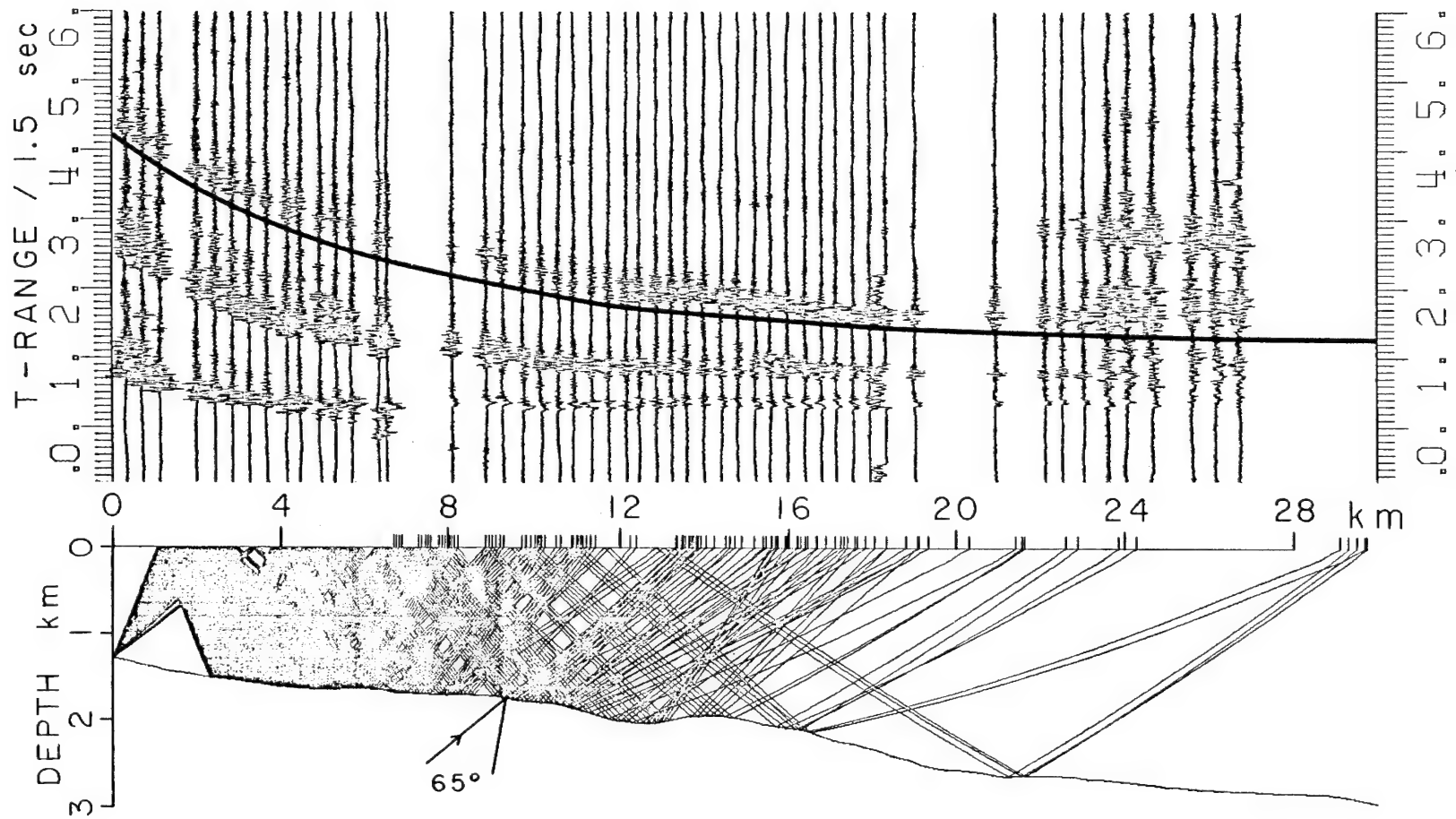


Fig. 18. Double bottom bounce ray paths from TOBS 3. The second bounce achieves critical incidence of  $65^\circ$  at around 9.5 km range on the bottom. The solid line precedes the second bottom bounce arrivals.

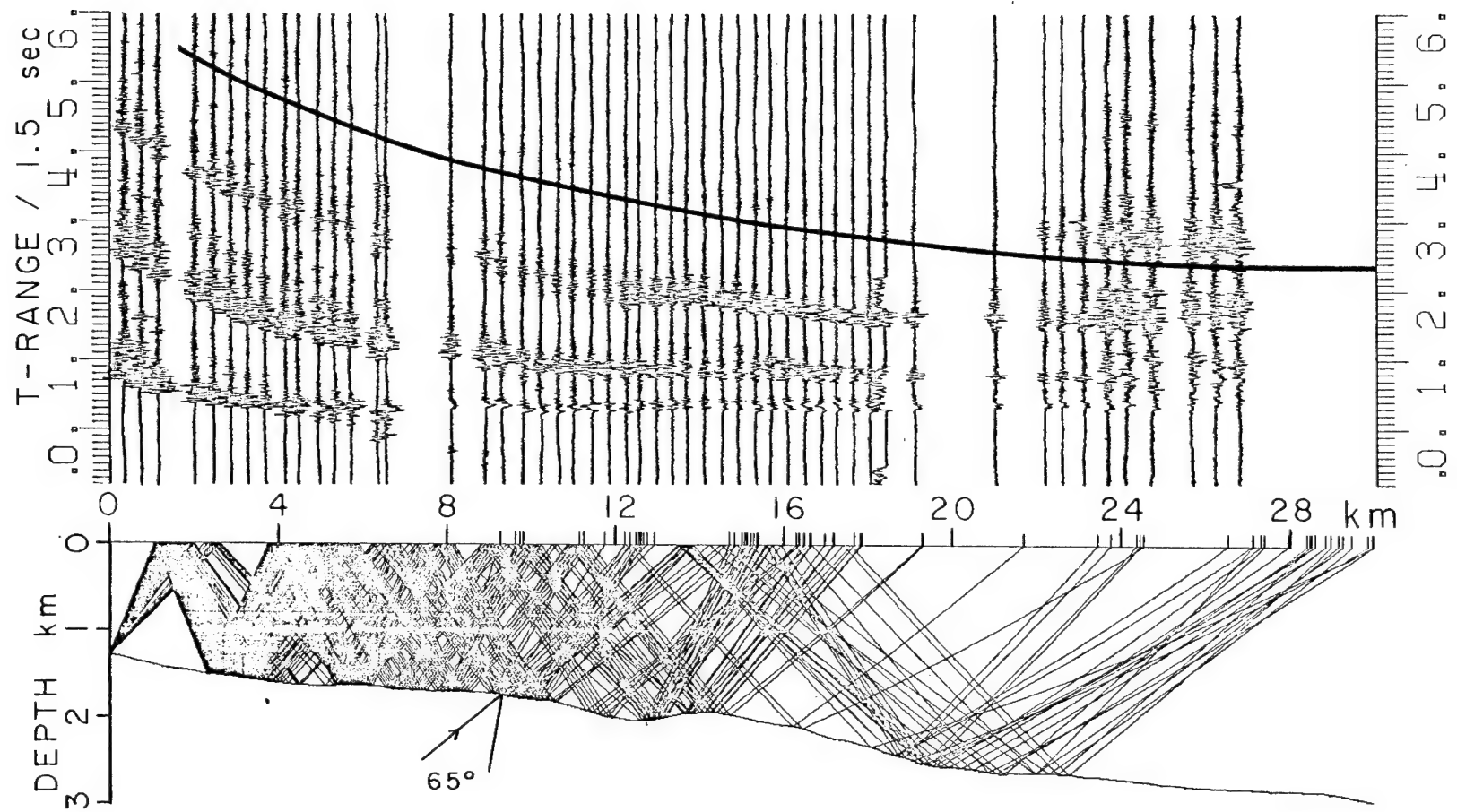


Fig. 19. Triple bottom bounce ray paths from TOBS 3. The solid line precedes the third bottom multiple arrivals.

## APPENDIX C. HEAD WAVE

A phase reversal at short range was observed in the onset of explosive signals received by TOBS 3 from large 1.8 lb (0.82 kg) SUS charges. The large SUS charge line was along the small SUS charge line of Figure 2 and extended upslope from the receiver. The shots were set off at 18 m depth and were recorded in water 1301 m deep.

Inspection of the first breaks in the first arrivals reveals a phase reversal (Figure 20) at shots with ranges of 2.0 and 3.8 km upslope and downslope from TOBS 3, respectively. It is probable that the phase change indicates the onset of a critically incident head wave. The developments below assume that the upslope and downslope phase reversals mark rays that impinge upon the bottom at the same incidence angle (Figure 21). This incidence angle is the critical angle, from which the sediment velocity may be computed if the water velocity is known.

By assuming a direct water borne path from a shot near the surface to the receiver on the ocean bottom, the ray parameter corresponding to the travel time of a first arrival may be calculated. The water velocity structure on the left side of Figure 3, extrapolated linearly down to 1301 m, is used for this calculation. For the water velocity structure and the shot ranges under consideration, it happens that each travel time corresponds to a unique ray parameter. The ray parameter is computed from the following arrangement of a well known formula;

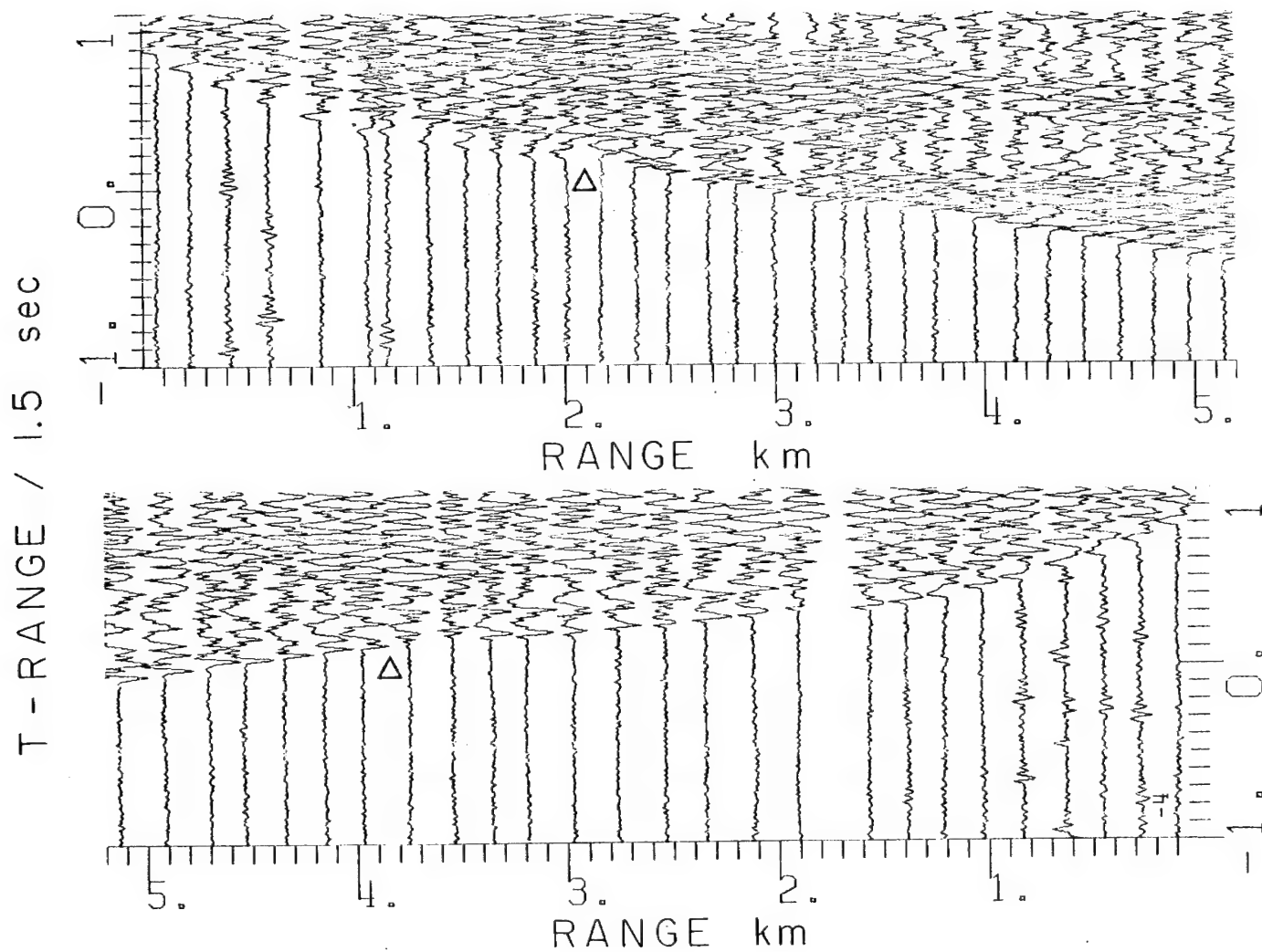
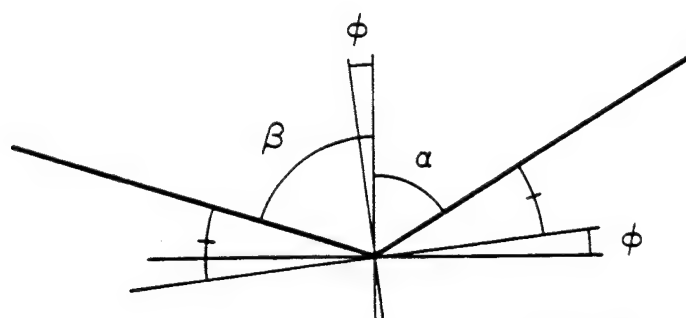
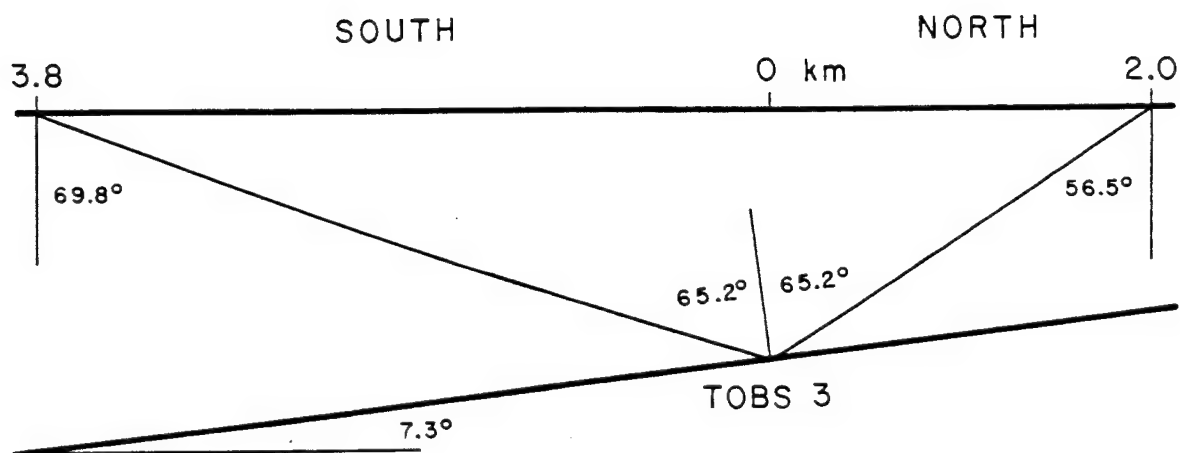


Fig. 20. Above: Large SUS charge shots originating upslope from TOBS 3.  
 Below: Shots originating downslope from TOBS 3.  
 The triangles denote the phase reversal in the first break.



$$\alpha = 57.9^\circ$$

$$\beta = 72.5^\circ$$

$$2\phi = \beta - \alpha, \phi = 7.3^\circ$$

$$\alpha + \phi = \beta - \phi = 65.2^\circ$$

Fig. 21. Top: Geometry for ray paths occurring at  $65.2^\circ$  critical incidence.

Bottom: Bottom angles  $\alpha$  and  $\beta$  are computed from their corresponding ray parameters and the bottom water velocity, 1488 m/s.  $\phi$  is the bottom slope in the vicinity of TOBS 3 and may be computed from  $\alpha$  and  $\beta$ . Using  $\phi$  and  $\alpha$  or  $\beta$ , the  $65.2^\circ$  incident angle with respect to the bottom is determined.

$$T - \int_{z_0}^D \frac{\eta^2}{(\eta^2 - p^2)^{1/2}} dz = 0, \quad [33]$$

where  $z_0$  = shot depth,  $D$  = bottom depth,  $T$  = travel time,  $\eta = 1/c(z)$ , and  $p = p(T)$  = ray parameter. Equation [33] may be solved for  $p$  by providing an initial guess for  $p$  and using the secant method or other root finding technique. The integrand is numerically integrated.

Once the ray parameter is found for the rays corresponding to the upslope and the downslope phase reversal, the ocean bottom slope and bottom incident angle associated with the phase reversal may be computed, as shown in Figure 21. This bottom incident angle is the critical angle.

The nature of the phase reversal is investigated further by examining the first break amplitudes. The ray parameter for each shot is obtained using equation [33]. From each ray parameter, the bottom incident angle and horizontal range are calculated. First break amplitudes for shots downslope from the receiver versus bottom incident angle and horizontal range are plotted in Figure 22. The expected amplitude decay due to spherical spreading is also indicated in the figure. The failure of shots closer than 1600 m to obey spherical spreading suggests that the near shot first breaks saturated the recording amplifier. The phase reversal occurs abruptly just past  $65^\circ$  bottom incidence, signaling the onset of the head wave. Beyond  $65^\circ$ , the first arrival is no longer the direct wave in the water so that the computed incident angles and ranges no longer apply. This fact is illustrated in the lower part of Figure 22. Shown is the difference

between horizontal ranges based on equation [33] ray parameters and horizontal ranges obtained from shipboard navigation. The sudden drop off beyond  $65^{\circ}$  incidence indicates that the computed ray parameters no longer describe the first arrival, which is no longer a water borne direct wave. The same results are obtained by looking at the first break amplitudes for shots upslope of the TOBS (Figure 23). In this case, the head wave onset is indicated by a sharp upward swing of the range difference plot.

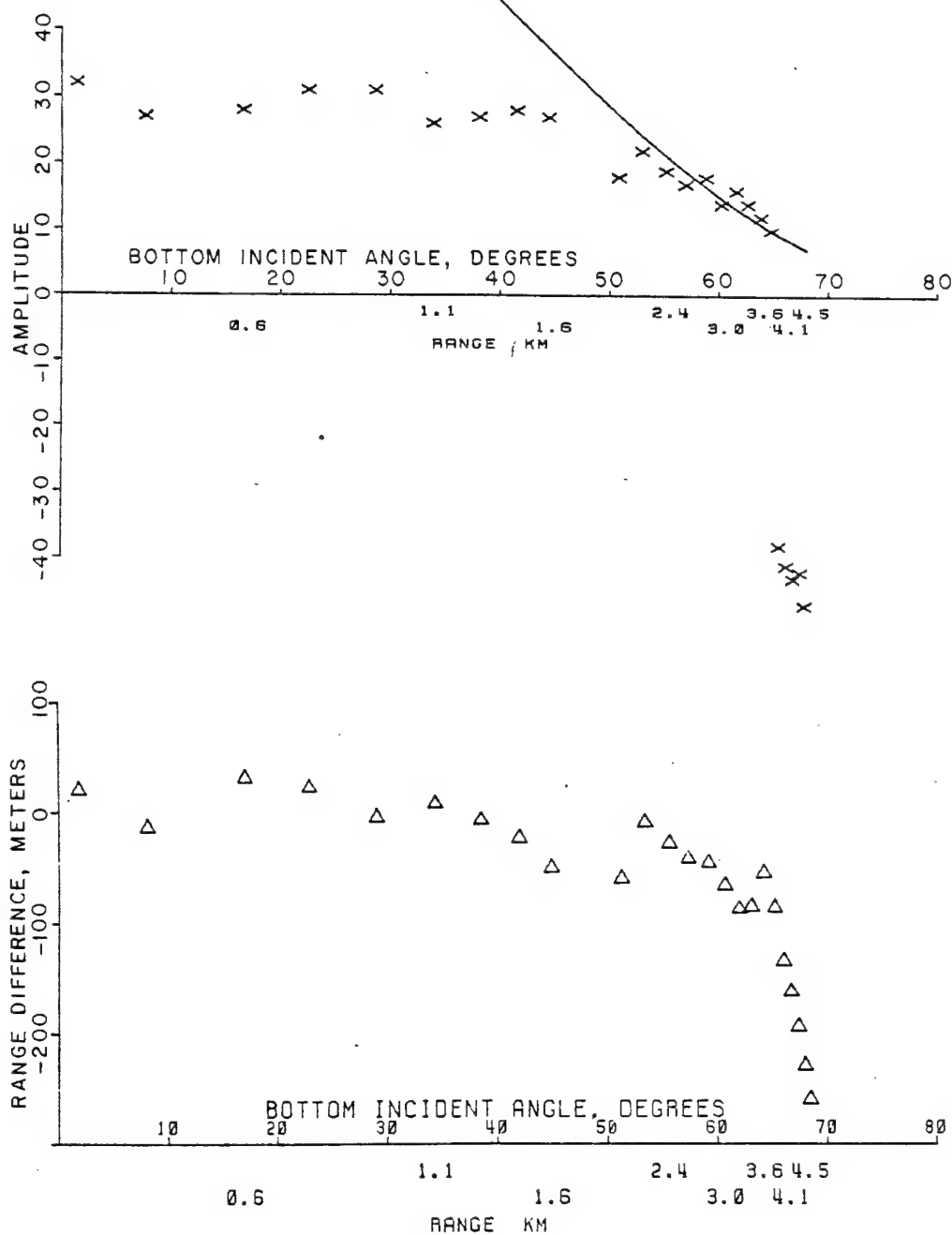


Fig. 22. Above: First break amplitudes versus computed bottom incident angle and horizontal range of raypath. The shots are downslope from the receiver. Solid line is loss caused by spherical spreading, normalized on the last shot before the phase reversal. Below: Difference between the computed horizontal range and the range from shipboard navigation versus calculated bottom incident angle.



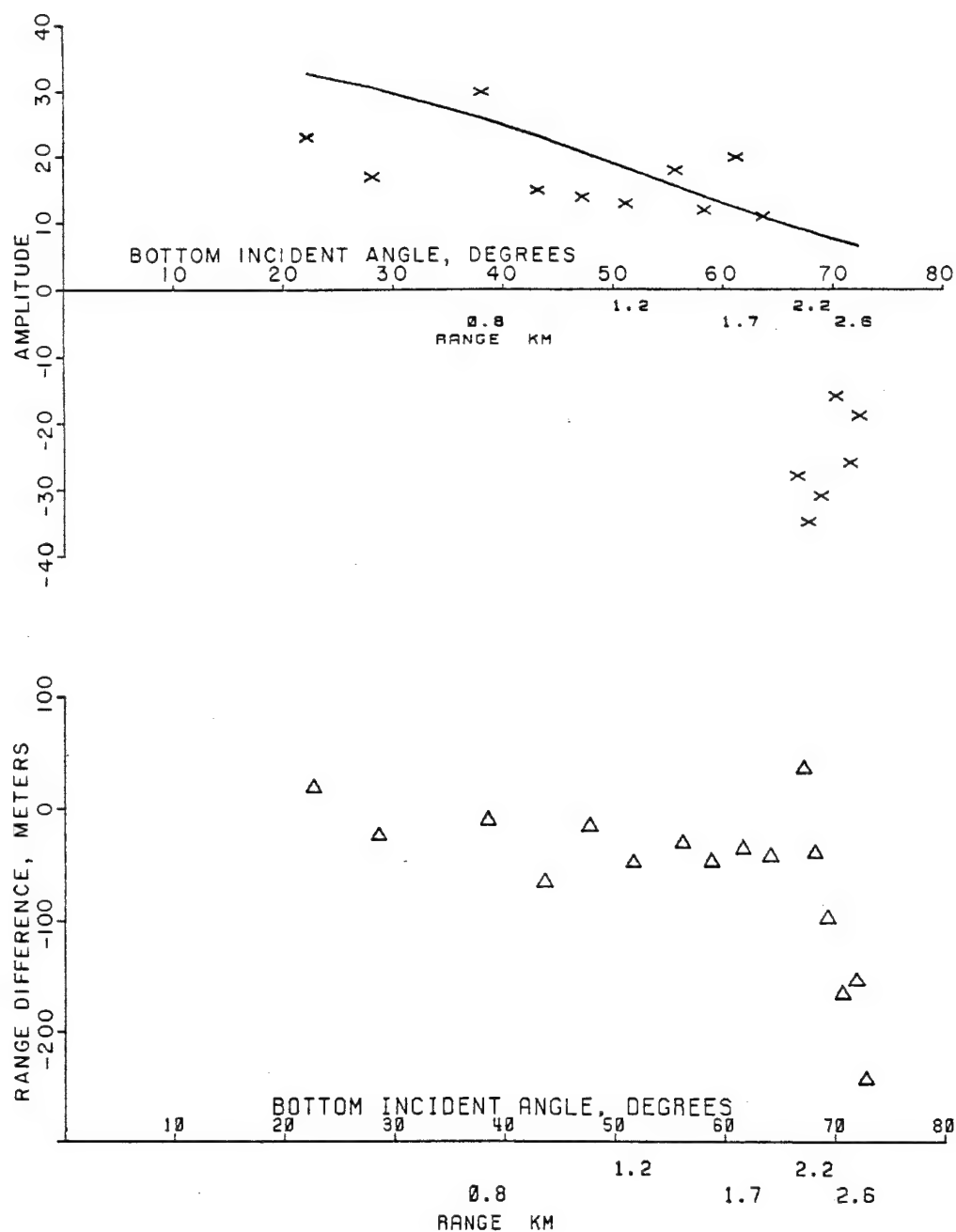


Fig. 23. Above: First break amplitudes versus computed bottom incident angle and horizontal range of raypath for shots upslope from the receiver. Solid line is spherical spreading loss, normalized on the last shot before the phase reversal. Below: Difference between the computed horizontal range and the range from shipboard navigation versus calculated bottom incident angle.

#### APPENDIX D. SEDIMENT VELOCITY FROM APPARENT VELOCITIES

The apparent velocities measured from the leading and trailing edges of the water wave, as shown in Figure 12, may be used to estimate the ocean bottom sediment velocity. The method for doing so was developed by Sutton and Maynard [1971] and described by Houtz [1980]. The technique is recapitulated here.

Consider a single shot. Let  $v_w$  be the water velocity and  $v_s$  be the bottom velocity. Let  $t_D$  be the travel time of the direct wave which is at the leading edge of the water wave. The travel time of the back end of the water wave is  $t_c$ . This arrival corresponds to the ray traveling at critical incidence  $\theta_c$  with respect to the bottom (Figure 24). It is assumed that the bottom sediment velocity is greater than the water velocity. The apparent velocity of the terminal arrival is  $v_g = v_w t_D / t_c$ . From Figure 24 the length  $AB = v_w t_D$ , and  $AB = v_w t_c \sin \theta_c$ . Using the above relations, one may write:

$$\sin \theta_c = \frac{t_D}{t_c} = \frac{v_g}{v_w} . \quad [34]$$

From Snell's law,

$$v_s = \frac{v_w}{\sin \theta_c} . \quad [35]$$

Replacing  $\sin \theta_c$  yields the result:

$$v_s = v_w^2 / v_g . \quad [36]$$

From Figure 12  $v_w = 1.42$  km/s and  $v_g = 1.32$  km/s. Using equation [36],  $v_s = 1.53$  km/s. This velocity is a bit lower than Scotian shelf values of 1.57 to 1.66 km/s measured by McKay and McKay [1982]. The slope correction given by Houtz [1980] is negligible for this example. One source of error may be the assumption of constant water velocity. The near surface gradient in the water velocity versus depth shown in Figure 13 hastens the arrival of the critically reflected wave so that  $\sin \theta_c$  of equation [34] is inflated. The increased  $\sin \theta_c$  produces a lower calculated sediment velocity  $v_s$ , as shown in equation [35].

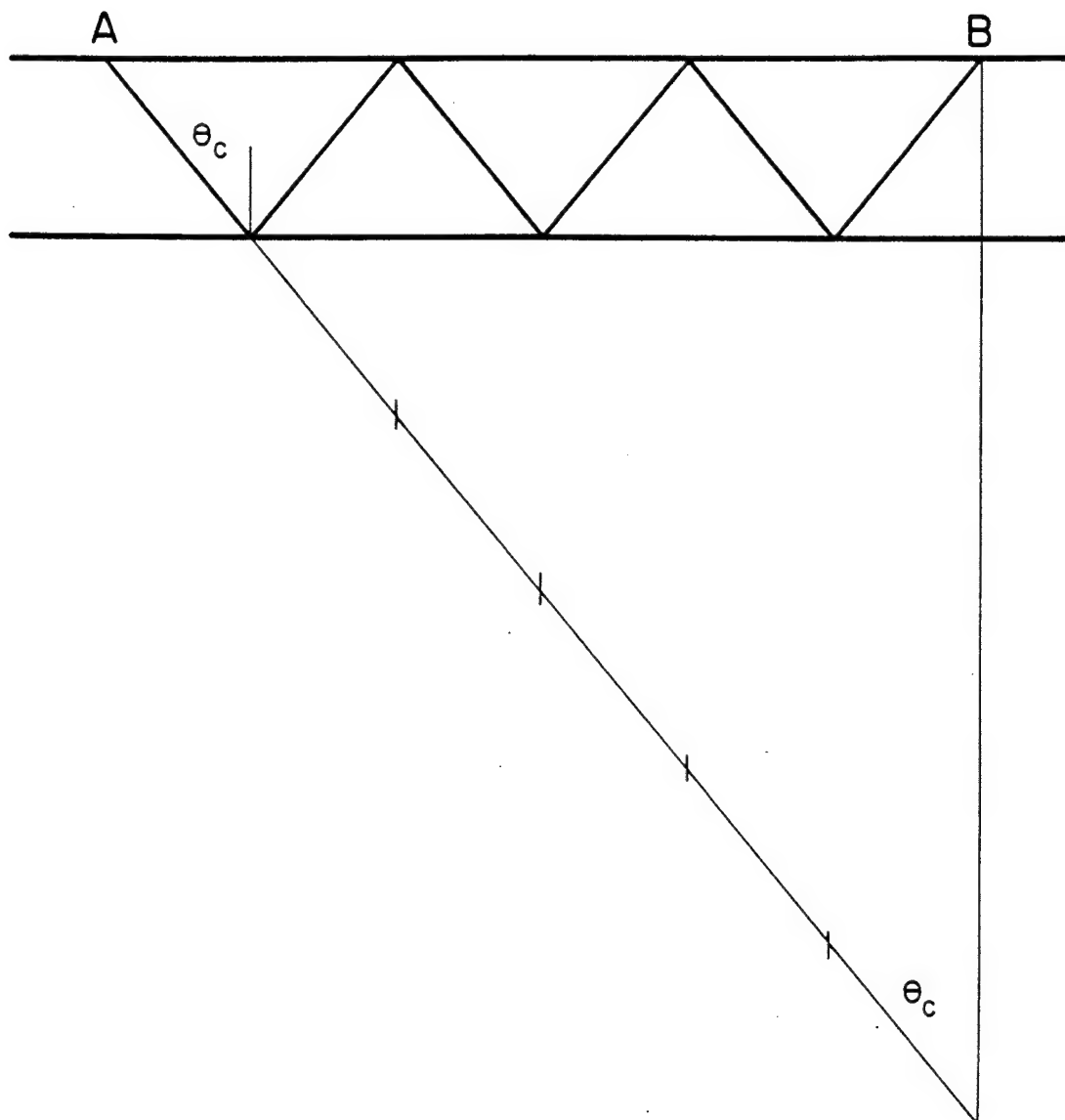


Fig. 24. Raypath at critical incidence  $\theta_c$ . The last arrival in the water wave travels at critical incidence.  $c$ . The total distance traveled is the hypotenuse of the large triangle, or  $v_w t_c$  (see text).

## REFERENCES

- Aki, K., and P. G. Richards, Quantitative Seismology, vol. 1, W. H. Freeman, San Fransisco, p. 169, 1980.
- Beebe, J. H., and S. T. McDaniel, Geoacoustic models of the seabed to support range-dependent studies on the Scotian shelf, Bottom-Interacting Ocean Acoustics, edited by W. A. Kuperman and F. B. Jensen, Plenum, New York, pp. 507-523, 1980.
- Brekhovskikh, L. M., Waves in Layered Media, 2nd ed., Academic, New York, 1980.
- Brocher, T. M., Iwatake, B. T., Gettrust, J. F., Sutton, G. H., and L. N. Frazer, Comparison of the S/N ratios of low-frequency hydrophones and geophones as a function of ocean depth, *Bull. Seism. Soc. Am.*, 71, pp. 1649-1659, 1981.
- Brock, H. K., Buchal, R. N., and C. W. Spofford, Modifying the sound-speed profile to improve the accuracy of the parabolic-equation technique, *J. Acoust. Soc. Am.*, 62, pp. 543-552, 1977.
- Brock, H. K., The AESD parabolic equation model, Naval Ocean Research and Development Activity TN 12, NSTL Station, Mississippi, 1978.
- Claerbout, J. F., Coarse grid calculations of waves in inhomogenous media with application to delineation of complicated seismic structure, *Geophysics*, 35, pp. 407-418, 1970a.
- Claerbout, J. F., Numerical Holography, in Acoustical Holography, vol. 3, edited by A. F. Methesell, Plenum, pp. 273-283, 1970b.
- Clay, C. S., and H. Medwin, Acoustical Oceanography, John Wiley, New York, pp. 59, 97, 1977.
- Clayton, R. W., and B. Engquist, Absorbing boundary conditions for acoustic and elastic wave equations, *Bull. Seism. Soc. Am.*, 67, pp. 1529-1540, 1977.
- Corones, J., Bremmer series that correct parabolic approximations, *J. Math. Anal. and Appl.*, 50, pp. 361-372, 1975.
- DiNapoli, F. R., and R. L. Deavenport, Numerical models of underwater acoustic propagation, in Ocean Acoustics, edited by J. A. DeSanto, Springer-Verlag, Berlin, p. 138, 1979.

- Fitzgerald, R. M., Helmholtz equation as an initial value problem with application to acoustic propagation, *J. Acoust. Soc. Am.*, 57, pp. 839-842, 1975.
- Frisk, G. V., Douth, J. A., and E. E. Hays, Bottom interaction of low-frequency acoustic signals at small grazing angles in the deep ocean, *J. Acoust. Soc. Am.*, 69, pp. 84-94, 1981.
- Gerald, C. F., Applied Numerical Methods, Addison-Wesley, Reading, pp. 98,193,204, 1970.
- Graves, R. D., Nagl, A., Uberall, H., and G. L. Zarur, Range-dependent normal modes in underwater sound propagation: Application to the wedge-shaped ocean, *J. Acoust. Soc. Am.*, 58, pp. 1171-1177, 1975.
- Hamilton, E. L., Compressional-wave attenuation in marine sediments, *Geophysics*, 37, pp. 620-646, 1972.
- Hamilton, E. L., Sound velocity gradients in marine sediments, *J. Acoust. Soc. Am.*, 65, pp. 909-922, 1979.
- Hamilton, E. L., Geoacoustic modeling of the sea floor, *J. Acoust. Soc. Am.*, 68, 1313-1340, 1980.
- Hanna, J. S., Example of acoustic model evaluation and data interpretation, *J. Acoust. Soc. Am.*, 60, pp. 1024-1031, 1976.
- Hanna, J. S., and P. V. Rost, Parabolic equation calculations versus North Pacific measurement data, *J. Acoust. Soc. Am.*, 70, pp. 504-515, 1981.
- Hood, P., Finite difference and wave number migration, *Geophys. Prosp.*, 26, pp. 773-789, 1978.
- Hornbeck, R. W., Numerical Methods, Quantum, New York, p. 97, 1975.
- Houtz, R. E., Seafloor and near-surface sound velocities from Barents Sea sonobuoy data, *J. Geophys. Res.*, 85, pp. 4838-4844, 1980.
- Jansa, L. F., and J. A. Wade, Geology of the continental margin off Nova Scotia and Newfoundland, in *Offshore Geology of Eastern Canada* vol. 2, *Geol. Surv. Can. paper* 74-30, pp. 51-104, 1974.
- Jensen, F. B., and W. A. Kuperman, Sound propagation in a wedge-shaped ocean with a penetrable bottom, *J. Acoust. Soc. Am.*, 67, pp. 1564-1566, 1980.
- King, L. H., and B. MacLean, Continuous seismic-reflection study of Orpheus gravity anomaly, *Am. Asso. Petr. Geologists Bull.*, 54, pp. 2007-2031, 1970.

- Lee, D., and J. S. Papadakis, Numerical solutions of underwater acoustic wave propagation problems, Naval Underwater Systems Center tech. rept. 5929, 1979.
- Lee, D., Botseas, G., and J. S. Papadakis, Finite-difference solution to the parabolic wave equation, J. Acoust. Soc. Am., 70, pp. 795-800, 1981.
- Lee, D. and K. E. Gilbert, Recent progress in modeling bottom-interacting sound propagation with parabolic equations, Naval Oceanographic Research and Development Activity, NSTL Station MS 39529, July 1982.
- Luke, Y. L., The Special Functions and Their Approximations, vol. 2, Academic, New York, p. 304, 1969.
- McDaniel, S. T., Propagation of a normal mode in the parabolic approximation, J. Acoust. Soc. Am., 57, pp. 307-311, 1975a.
- McDaniel, S. T., Parabolic approximations to underwater sound propagation, J. Acoust. Soc. Am., 58, pp. 1178-1185, 1975b.
- McDaniel, S. T., and D. Lee, A finite-difference treatment of interface conditions for the parabolic wave equation: The horizontal interface, J. Acoust. Soc. Am., 71, pp. 855-858, 1982.
- McKay, A. G., and P. M. McKay, Compressional-wave velocity measurement in seabed materials by use of equipment deployed near, but above the bottom, J. Acoust. Soc. Am., 71, pp. 871-878, 1982.
- Mitchell, A. R., and D. W. Griffiths, The Finite Difference Method in Partial Differential Equations, John Wiley, Chichester, p. 29, 1980.
- Morris, H. E., Hamilton, E. L., Buckner, H. P., and R. T. Bachman, Interaction of sound with the ocean bottom, Naval Ocean Systems Center tech. rept. 242, 1978.
- Officer, C. B., Intro. to the Theory of Sound Transmission, McGraw-Hill, New York, p. 77, 1958.
- Parrott, D. R., Dodds, D. J., King, L. H., and P. G. Simpkin, Measurement and evaluation of the acoustic reflectivity of the sea floor, Can. J. of Earth Sciences, 17, pp. 722-737, 1980.
- Piper, D. J. W., Late Quaternary deep water sedimentation off Nova Scotia and western Grand Banks, Can. Soc. Petr. Geologists, Memoir 4, pp. 195-204, 1977.

- Sheriff, R. E., Encyclopedic Dictionary of Exploration Geophysics, Soc. of Exploration Geophysicists, Tulsa, 1973.
- Stoll, R. D., Acoustic waves in saturated sediments, in Physics of Sound in Marine Sediments, edited by L. Hampton, Plenum, New York, 1974.
- Sutton, G. H. and G. L. Maynard, Ocean-bottom sediment velocity determined from critical range multiple reflections (abstract), Eos Trans. AGU, 52, p. 4, 1971.
- Sutton, G. H., Kasahara, J., Ichinose, W. N., and D. A. Byrne, Ocean bottom seismograph development at Hawaii Institute of Geophysics, Marine Geophysical Researches, 3, pp. 153-157, 1977.
- Tappert, F. D., The parabolic approximation method, in Wave Propagation and Underwater Acoustics, edited by J. B. Keller and J. S. Papadakis, Springer-Verlag, Berlin, pp. 224-287, 1977.
- Vidmar, P. J., The dependence of bottom reflection loss on the geoacoustic parameters of deep sea (solid) sediments, J. Acoust. Soc. Am., 68, pp. 1442-1453, 1980.
- Volk, P. M., Solutions of acoustic wave propagation in the ocean by the parabolic approximation to the wave equation, master's thesis, Oceanography Department, University of Hawaii, Honolulu, 1975.
- Wood, D. H., and J. S. Papadakis, Initial data for the parabolic equation, Bottom-Interacting Ocean Acoustics, edited by W. A. Kuperman and F. B. Jensen, Plenum, New York, pp. 417-420, 1980.